GEEA
Research article
Geochemistry: Exploration, Environment, Analysis
Published Online First, updated version
https://doi.org/10.1144/geochem2016-007

Vibrational spectroscopy of epidote, pumpellyite and prehnite applied to low-grade regional metabasites

Alistair J. R. White[1*], Carsten Laukamp[1], Mark A. Stokes[1,2], Monica Legras[1] & Bobby Pejcic[3]

[1] CSIRO Mineral Resources, Australian Resources Research Centre, 26 Dick Perry Avenue, Kensington, WA 6151, Australia
[2] School of Earth and Environmental Sciences, James Cook University, Building 34 James Cook Drive, Douglas, Qld 4811, Australia
[3] CSIRO Energy, Australian Resources Research Centre, 26 Dick Perry Avenue, Kensington, WA 6151, Australia
A.J.R.W., 0000-0003-3256-1171
*Correspondence: alistair.white@csiro.au

Abstract: Calc-silicate minerals are routinely used to identify metamorphic and metasomatic patterns, but their characterization usually requires detailed and time-consuming petrographic and geochemical analyses, preventing spatially extensive mapping. Laboratory measurements (FTIR, XRD, EPMA) successfully characterize pure representatives of three calc-silicate mineral groups – epidote, pumpellyite, and prehnite – as well as mixed mineral samples from the Fortescue Group volcanics, Hamersley Basin, Western Australia. Pure mineral spectra display diagnostic first overtone bands of the hydroxyl-related stretching fundamentals in the 1300 – 1600 nm wavelength region. In mixed mineral assemblages the overtone region allows for identification based on discrete absorption bands: 1555 nm for epidote, 1470 nm for prehnite, and four bands at 1410 (a), 1430 (b), 1450 (c) and 1510 nm (d) for pumpellyite. With increasing Fe content, the wavelength positions of the hydroxyl-stretching fundamental and first overtone absorption features of epidote and prehnite shift towards shorter wavelengths. In pumpellyite, with increasing Mg content, bands (b) and (d) shift towards longer and shorter wavelengths respectively. Diagnostic overtones are identifiable after downsampling of laboratory FTIR spectra to hyperspectral field, airborne, and orbital spectrometer resolution. This highlights the application to regional-scale mapping of calc-silicate distribution and composition, both on Earth and on extraterrestrial planetary surfaces, such as Mars.

Keywords: Infrared spectroscopy; XRD; EPMA; Low-grade metamorphism; Hamersley Basin

Received 28 September 2016; **revised** 13 March 2017; **accepted** 26 March 2017

Calc-silicate minerals, hydrous silicate phases containing significant Ca, such as prehnite, pumpellyite, epidote and calcic amphiboles, constitute major components of low grade, regionally metamorphosed mafic rocks. The appearance of successive calc-silicate phases during prograde regional metamorphism has long been used to define a number of low-grade metamorphic facies: prehnite-pumpellyite, pumpellyite-actinolite, epidote-actinolite and amphibolite facies (Packham & Crook 1960; Smith *et al.* 1982; Schmidt *et al.* 1997). Additionally, these same minerals commonly form as a result of hydrothermal alteration of mafic rocks on the sea floor (Humphris & Thompson 1978), below the sea floor (Evarts & Schiffman 1983; Alt *et al.* 1986; Banerjee *et al.* 2000), or through metasomatism during metamorphism (Smith 1968; Engvik *et al.* 2011). When such hydrothermal alteration results in formation of an ore deposit, the abundance and composition of calc-silicates, and other infrared active minerals, can be useful exploration indicators (White *et al.* 2010; Roache *et al.* 2011; Laukamp *et al.* 2012).

Vibrational modes of the hydroxyl groups in common calc-silicate minerals produce diagnostic absorption features in the infrared part of the electromagnetic spectrum. These modes include (1) fundamental stretching vibrations in the mid-infrared (MIR) range (2500 – 25 000 nm; 4000 – 400 cm^{-1}); and (2) hydroxyl-group related overtone and combination bands in the short wave infrared (SWIR) range (1350 – 2500 nm; 7400 – 4000 cm^{-1}). Current hyperspectral field portable, drill core scanning and remote sensing technologies provide an opportunity to rapidly and reliably identify calc-silicates, and other infrared active minerals, and thereby determine metamorphic grade and/or extent of hydrothermal alteration in a range of rock types (Hermann *et al.* 2001; van Ruitenbeek *et al.* 2005, 2006; Swayze *et al.* 2009; Doublier *et al.* 2010; White *et al.* 2010; Laukamp *et al.* 2011*a*, *b*, 2012; Roache *et al.* 2011; Sonntag *et al.* 2012). Specifically, Roache *et al.* (2011) documented shifts in epidote composition associated with different hydrothermal alteration assemblages at St. Ives gold mine, Western Australia. Further comparison with stable isotope data suggested that the epidote composition was effectively mapping paleoredox gradients. Similar approaches have been developed utilizing the infrared spectra of chlorite and K-white micas in metapelitic rocks (van Ruitenbeek *et al.* 2006; Doublier *et al.* 2010, 2012; Duke & Lewis 2010).

In this paper, we present mid infrared (MIR) and short wave infrared (SWIR) spectra, X-ray diffraction (XRD) and electron probe microanalyser (EPMA) data for epidotes, pumpellyites and prehnites in a range of mixed mineral samples from the Fortescue Group volcanics, Hamersley Basin, Western Australia, together with a number of pure mineral samples from a variety of locations. Diagnostic SWIR features have already been documented for epidote (Hunt *et al.* 1973; Clark *et al.* 1990*a*; Roache *et al.* 2011). Here we define features for prehnite and pumpellyite and assess their wavelength positions for sensitivity to changing mineral composition and modal abundance in mixed mineral samples using infrared proximal and remote sensing technologies.

Vibrational spectroscopy and crystal chemistry of epidote, pumpellyite and prehnite

Fundamental stretching vibrations of M–O–H hydroxyl bonds, ν(OH), in calc-silicates occur in the mid-infrared 2500 – 3300 nm (3000 – 4000 cm^{-1}) wavelength region (e.g. Strens 1974). The first

overtones of the fundamental hydroxyl-stretching vibrations, 2ν(OH), occur in the SWIR wavelength region between 1350 – 1650 nm (6050 – 7400 cm^{-1}). Fundamental bending vibrations of M–O–H hydroxyl bonds, δ(OH), occur in the region around 14 285 – 25 000 nm (400 – 700 cm^{-1}) (e.g. Langer & Raith 1974). Stretch plus bend combination vibrations, δ + ν(OH), occur in the SWIR range at around 2250 nm (4445 cm^{-1}) and 2340 nm (4275 cm^{-1}) (Roache *et al.* 2011). While this range can be highly diagnostic of a range of common silicate minerals, the δ + ν(OH) absorption features of different minerals can strongly overlap and interfere, such that using this region to confidently determine proportions and compositions of phases in mineral mixtures is non-trivial. In this paper we focus predominantly on the fundamental stretching vibrations and their first overtones as these were ultimately determined to be the most useful for the identification and characterization of epidote, pumpellyite and prehnite. However, brief mention will be made of the combinations. Since the primary attention of this paper is on mixed mineral samples, we have prioritised mineral identification in the 2ν(OH) region, which avoids many of the issues of overlapping absorption features.

The exact frequency of vibration is affected by the bond environment of the hydroxyl group, such as the type of cation bonded to the protonated oxygen or the presence of additional H-bonds to neighbouring non-protonated oxygen atoms. Vibrational frequency is controlled by a complex interplay between various physiochemical characteristics of the bonded cation, such as electronegativity, ionic radius, cation charge and cation mass (Martínez-Alonso *et al.* 2002). Where hydrogen bonds are involved, a lengthening of the total O–H···O bond length results in higher stretching vibrational frequencies (shorter wavelengths) of the hydroxyl group (Bellamy & Owen 1969).

Epidote

The crystal chemistry and infrared spectroscopic characteristics of epidote have been well described (Dollase 1968; Gabe *et al.* 1973; Langer & Raith 1974; Clark *et al.* 1990*a*; Bonazzi & Menchetti 1995; Makreski *et al.* 2007; Roache *et al.* 2011). Epidotes are therefore investigated in this study primarily as a control mineral to confirm the various techniques used and to provide context to understanding the results from pumpellyite and prehnite. The ideal formula for the epidote group minerals is $A_2M_3[T_2O_7][TO_4](O,F)(OH,O)$, where A = Ca, ($Mn^{2+}$, Sr, Pb, REE), M = Al, Fe^{3+}, (Mn^{3+}, V^{3+}, Cr^{3+}, Fe^{2+}) in octahedral coordination, and T = tetrahedral sites containing Si or Al (Bonazzi & Menchetti 1995; Armbruster *et al.* 2006). One of the most common element substitutions in epidote is the exchange of Fe^{3+} for Al leading to the solid solution series between clinozoisite, $Ca_2Al_3Si_3O_{11}(OH)$, and a notional 'pistacite' end-member $Ca_2Fe_3Si_3O_{11}(OH)$. Structurally, octahedra are arranged in two chains: the first comprises edge sharing M1 octahedra with M3 octahedra alternately added to either side to form a 'zigzag' arrangement; the second comprises just edge sharing M2 octahedra (Fig. 1; Dollase 1968). Consequently, M1, M2 and M3 have different sizes, and as such, Fe^{3+} preferentially enters M3, followed by M1, while M2 almost exclusively contains Al (Gabe *et al.* 1973; Bonazzi & Menchetti 1995; Giuli *et al.* 1999). Lattice parameters correlate with Fe content such that *a, b* and *c* increase with increasing Fe, while *β* decreases slightly (Franz & Liebscher 2004). The lengths of *a* and *c* increase with approximately the same magnitude, while *b* increases by approximately a factor of two greater. There is a slight change in this correlation gradient at around Xep = 0.6 – 0.7 (Xep = $Fe^{3+}/[Al + Fe^{3+} + Cr^{3+} - 2]$), which corresponds to the substitution of Fe at the M1 site at high Fe contents. These changes in structural parameters produce a lengthening of individual M–O bonds within all M site octahedra (Bonazzi & Menchetti 1995; Giuli *et al.* 1999), as well as a lengthening of the O10–H···O4 hydrogen bond (Fig. 1; Langer & Raith 1974; Bonazzi & Menchetti 1995).

Vibrational spectroscopy of epidote group minerals exhibits a single ν(OH) fundamental in the range 3326 – 3365 cm^{-1} (2970 – 3006 nm), which shifts towards higher frequencies (shorter wavelengths) with increasing Fe content (Langer & Raith 1974). The first overtone, 2ν(OH), of this fundamental vibration occurs at around 6410 – 6495 cm^{-1} (1540 – 1560 nm), with the same shift towards shorter wavelengths at higher Fe contents (Roache *et al.* 2011). These shifts are primarily due to lengthening of the O10–H···O4 bond, caused by lattice expansion, despite the effect of increasing electronegativity when Fe^{3+} substitutes for Al (Langer & Raith 1974).

Pumpellyite

The ideal formula of pumpellyite is given by $W_4X_2Y_4Z_6O_{(20+x)}(OH)_{(8-x)}$, where W = Ca, (Na, K, Mn); X = $[Mg, Fe^{2+}, Mn^{2+}]_{2-x}$ $[Fe^{3+}, Al, (Mn^{3+}, Cr^{3+}, V^{3+})]_x$; Y = Fe^{3+}, Al, (Mn^{3+}, Cr^{3+}, V^{3+}, Ti); Z = Si (Passaglia & Gottardi 1973; Coombs *et al.* 1976). Pumpellyite is crystallographically related to epidote with two independent chains of edge sharing octahedra (Fig. 2; Yoshiasa & Matsumoto 1985; Nagashima *et al.* 2010). Pumpellyite is commonly idealized as containing divalent cations at half of the X sites ($x = 1$ in the formula given above) (Coombs *et al.* 1976; Nagashima *et al.* 2010). Pumpellyite contains four hydroxyl sites if X contains only divalent cations (Fig. 2), but only three if X is filled by trivalent cations (Fig. 2), as required for charge balance (Nagashima *et al.* 2010). All of these hydroxyl sites involve additional hydrogen bonds, many of which are also bifurcated (Fig. 2). These hydrogen bond combinations are given in Table 1. O5 and O7 in this scheme are located at the corners of the Y site octahedra that are not bonded to neighbouring tetrahedral sites. O11 is similarly located at the X site octahedra, whereas O10 is part of the cross-linking $Z_2O_6(OH,O)$ group.

As with epidote, a range of elemental substitutions is possible in pumpellyite. The most common are the exchange of divalent Fe^{2+} and Mg, and the exchange of trivalent Fe^{3+} and Al, forming a solid solution series between the idealised end-members pumpellyite-(Mg), $Ca_4MgAl_5Si_6O_{21}(OH)_7$, and julgoldite, $Ca_4Fe^{2+}Fe_5^{3+}Si_6O_{21}(OH)_7$ (Passaglia & Gottardi 1973). This Mg-Fe^{2+}-Fe^{3+} ternary system is the only compositional variation considered here as it covers the vast majority of compositional variation observed in natural systems (Springer *et al.* 1992; Potel *et al.* 2002; Ruiz Cruz *et al.* 2010; White *et al.* 2014*a*). Octahedral Y sites contain exclusively trivalent cations, whereas the larger X site contains both divalent and trivalent cations (Artioli & Geiger 1994; Nagashima *et al.* 2010). As with epidote, lattice parameters lengthen with increasing Fe content (Passaglia & Gottardi 1973), which lengthens the majority of individual M–O bonds and hydrogen-bonds (Nagashima *et al.* 2006).

Vibrational spectroscopic studies of pumpellyite have primarily focused on the fundamental modes in the MIR to allow for structural refinement of different pumpellyite phases (Hatert *et al.* 2007; Hamada *et al.* 2010; Nagashima *et al.* 2010). SWIR characterisation of hydroxyl related overtone and combination bands is effectively unknown. Several different ν(OH) features have been documented. Hatert *et al.* (2007) identified five vibrational features at frequencies of 3010, 3127, 3407, 3499 and 3542 cm^{-1} in a sample of pumpellyite-(Al). Hamada *et al.* (2010) identified four features at 2911, 3220, 3397 and 3512 cm^{-1} in a chromian pumpellyite. Finally, Nagashima *et al.* (2010) used attenuated total reflection methods (ATR-FTIR) to study another chromium-rich pumpellyite and identified two major features at 3522 and 3379 cm^{-1}, plus an 'additional broad band' at around 3100 cm^{-1}. Closer inspection of their spectrum (Fig. 2 of Nagashima *et al.* 2010) reveals that the broad band may contain at least two peaks, one around 3120 cm^{-1}

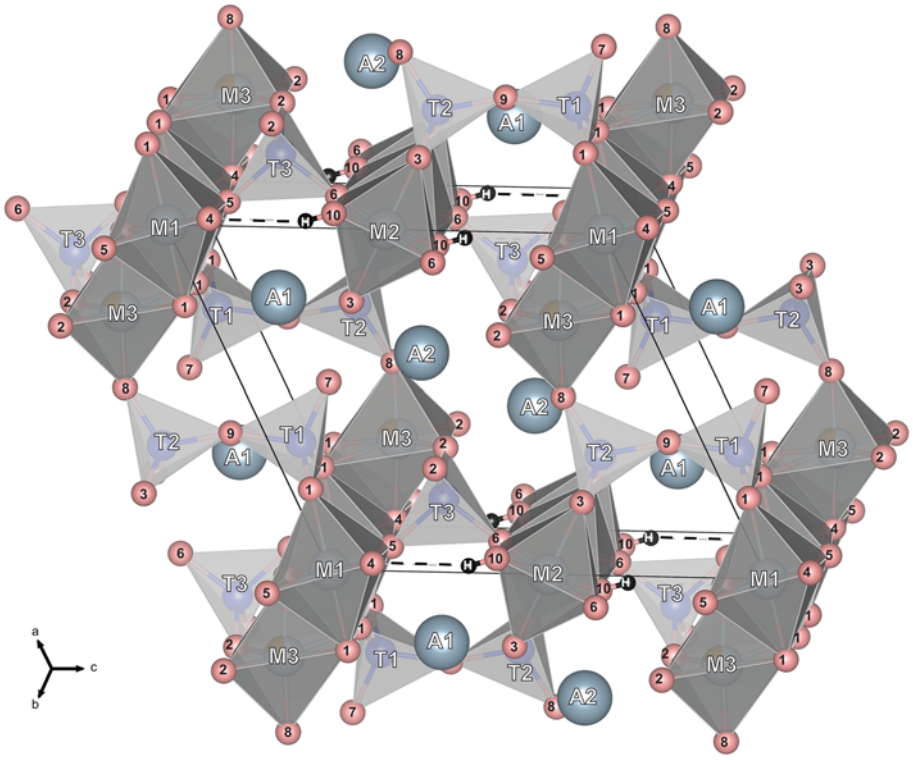

Fig. 1. Crystal structure of epidote, looking sub-parallel to [010]. Crystallographic data are from Comodi & Zanazzi (1997) and the projection was constructed using the VESTA 3 program of Momma & Izumi (2011). Hydroxyl groups are located at O10, with the hydrogen atom (black) forming an additional hydrogen bond to O4 (dashed line).

and the other at around 3050 cm^{-1}. Some of these features may be correlated between studies, although in some cases they would involve shifts of as much as 100 cm^{-1}. However, it is difficult to be certain due to the small data set, the wide variation in studied compositions, and the lack of relatively more common Mg- and Fe-rich samples.

Prehnite

Prehnite, $Ca_2(Al,Fe^{3+},Mn^{3+})AlSi_3O_{10}(OH)_2$, is an orthorhombic mineral consisting of double sheets of $(Al,Si)O_4$ and SiO_4 tetrahedra, forming Si_3AlO_{10} type sheets, extending parallel to (001) (Fig. 3; Detrie *et al.* 2008). These alternate and share oxygens with single sheets of linked $(Al,Fe^{3+},Mn^{3+})O_4(OH)_2$ octahedra. The alternating sheets create a channel in the structure parallel to [100] where Ca is located in [7]-fold coordination. The most common symmetry of prehnite is *Pncm*, although variations in ordering of Al and Si on the tetrahedral sites can produce *P*2*cm*, *P*2/*n*, and notional $P22_12$ symmetries (Detrie *et al.* 2008). The hydroxyl group is located at the octahedral site, but has a bifurcated hydrogen-bond with the two O1 oxygens shared by the neighbouring octahedra and tetrahedra (Fig. 3; Detrie *et al.* 2008).

In comparison to epidote and pumpellyite, the prehnites analysed in this study exhibit relatively little compositional variation. However, a common exchange is Fe^{3+} for Al at the octahedral site (Artioli *et al.* 1995; Akasaka *et al.* 2003). This is the only compositional variable considered here. As with epidote and pumpellyite, the inclusion of Fe into prehnite expands the crystal lattice, and lengthens the structural parameters and individual bonds (Detrie *et al.* 2008).

The infrared spectroscopy of prehnite is very poorly characterized. Gangi Reddy *et al.* (2005) recorded a sharp peak in the SWIR range at 7215 cm^{-1} (1386 nm), which they assigned to the first overtone of the hydroxyl group, 2ν(OH). Detrie (2008) identified a well-defined high intensity peak at 3490 cm^{-1} (2865 nm), which is the corresponding stretching fundamental, typically with a broad shoulder to lower frequencies. The United States Geological Survey spectral library splib06a (Clark *et al.* 2007) provides four spectra for prehnite with features at *c.* 1480 nm (6757 cm^{-1}) and 2875 nm (3478 cm^{-1}), that likely correspond to the first overtone and the fundamental of the hydroxyl stretch.

Sample collection

The mixed mineral samples used in this study come from mafic flood lavas belonging to the Fortescue Basin (2.8 – 2.4 Ga), which comprises the oldest component of the Mount Bruce Supergroup in the Hamersley Basin, located on the southern margin of the Pilbara

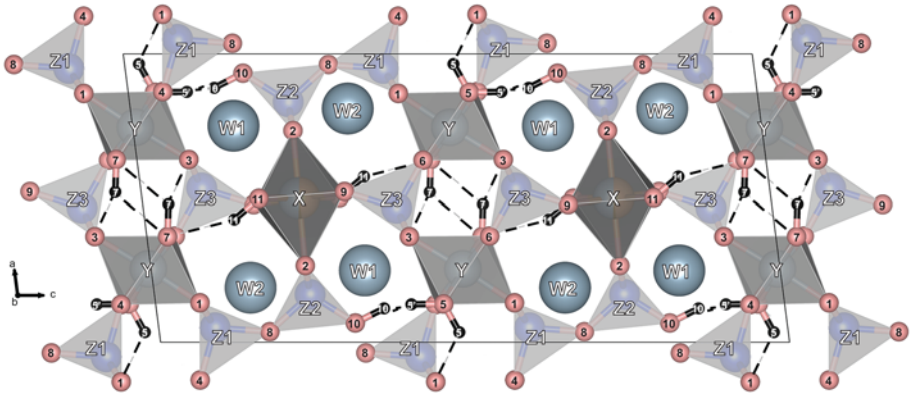

Fig. 2. Crystal structure of pumpellyite, looking parallel to [010]. Crystallographic data are from Nagashima *et al.* (2010) and the projection was constructed using the VESTA 3 program of Momma & Izumi (2011). Pumpellyite contains four distinct hydroxyl groups with a complex set of hydrogen bonds (dashed lines). If the X site octahedra are solely occupied by trivalent cations, the hydrogen atoms at H5 and H10 are replaced by one at H5′.

Table 1. *Hydrogen bonds in pumpellyite, as determined by Nagashima* et al. *(2010)*

Hydrogen Bond	Cations on X sites	
	All divalent cations	All trivalent cations
1	bifurcated O7–H7···O3 and O7–H7···O7	bifurcated O7–H7···O3 and O7–H7···O7
2	O11–H11···O7	O11–H11···O7
3	bifurcated O5–H5···O1 and O5–H5···O5	O5–H5′···O10
4	O10–H10···O5	

If only three hydroxyl sites are present then locations 3 and 4 are replaced by an O5–H5′···O10 arrangement.

Craton, Western Australia (Fig. 4; Trendall 1990; Thorne & Trendall 2001). A regional burial metamorphic gradient, defined by authigenic mineral growth in the Fortescue Group, extends across the Hamersley Basin from prehnite-pumpellyite facies in the north to greenschist facies in the south and west (Smith *et al.* 1982; White *et al.* 2014*a*, *b*). Four distinct metamorphic zones have been identified: zone 1 (ZI), prehnite–pumpellyite; ZII, prehnite–pumpellyite–epidote; ZIII, pumpellyite–epidote–actinolite–prehnite; ZIV, epidote–actinolite. Epidote shows a strong trend towards less Fe-rich compositions with increasing metamorphic grade, from ZII to ZIV (White *et al.* 2014*a*).

Superimposed on the regional metamorphic gradient are widespread zones of intense metasomatism (Smith *et al.* 1982; White *et al.* 2014*a*). These zones coincide with lava flow tops and extend for tens to hundreds of kilometres along strike. Metasomatic assemblages are characterized initially by the growth of visible patches of prehnite, which constitutes up to 10 volume % of the altered rock. As metasomatism progresses and fluid/rock ratio increases, the rocks are extensively replaced and recrystallised with quartz-epidote and quartz-pumpellyite dominated assemblages (White *et al.* 2014*a*, *b*). In highly altered rocks, epidote and/or pumpellyite comprise as much as 60 volume % of the rock. Metasomatism progressively overprints the earlier regional metamorphism and alteration assemblages are essentially independent of metamorphic grade. The observed mineralogical changes are the result of extensive changes in bulk rock chemistry, particularly the depletion of alkali metals, Mg, and the heavy first transition series metals (Mn–Zn) (White *et al.* 2014*a*).

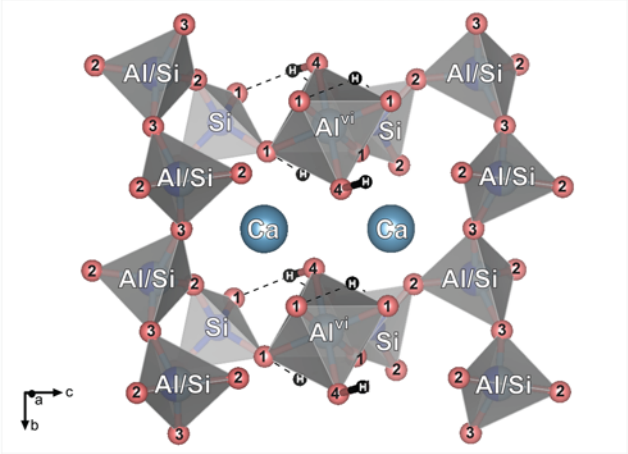

Fig. 3. Crystal structure of prehnite, looking sub-parallel to [100]. Crystallographic data are from Detrie *et al.* (2008) and the projection was constructed using the VESTA 3 program of Momma & Izumi (2011). Hydroxyl groups are located at O4 and hydrogen bonded to the O1 oxygens shared by the neighbouring octahedral and tetrahedral sites in the [100] direction (dashed line).

Regionally metamorphosed and hydrothermally altered mafic rocks of the Fortescue Group, including all samples used in this study, have already been investigated in detail, incorporating petrography, mineral and whole rock geochemistry and semi-quantitative X-ray diffraction (Smith *et al.* 1982; White 2013; White *et al.* 2014*a*, *b*). As such, a detailed description of sample petrography is not provided here, but can be obtained from the references above.

The pure mineral samples used in this study were provided by the Western Australian Museum and CSIRO's Mitchell Collection, located at the Australian Resources Research Centre, both sited in Perth, Australia. Although notionally pure single crystals or crystal fragments, a few of these samples did contain trace impurities of quartz and unidentified clay minerals. Sample locations, where known, are given in Table 2.

A combination of pure and mixed mineral samples is used in this study as each provides a different perspective on understanding the infrared spectral responses of these minerals. Specifically, pure mineral samples allow for the confident identification of characteristic absorption features, while the mixed mineral samples expand the available compositional range and provide a more reliable assessment of this technique when applied to natural systems, which commonly contain mineral mixtures. This approach has been used as initial investigations suggested the difference in wavelength position between characteristics absorption features is typically greater than any shift produced by compositional variation (see below).

Analytical methods

X-ray diffraction (XRD), mineral chemical and infrared spectral data were obtained for a subset of mixed mineral samples collected from the Fortescue Group, in addition to all pure mineral samples obtained from the sources listed above. Each sample in this subset was prepared as a polished thin section, with an accompanying piece from the immediately adjacent portion of rock pulverized to a homogeneous powder, before being analysed with all techniques given below to allow for a complete comparison between results. The subset was chosen to include representative samples distributed from metamorphic zones ZI – ZIV, and including both regional metamorphic assemblages and metasomatized rocks. Key results for all analysed samples are presented in Table 3 and discussed further below. XRD and mineral chemical data for mixed mineral samples from the Fortescue Group (HM-* samples) are freely available from the CSIRO Data Access Portal (White 2013).

Powder X-ray diffraction

X-ray diffraction patterns of powdered samples were collected with a Bruker D4 Endeavor instrument fitted with a Co tube, Fe filter, and a Lynxeye position-sensitive detector. The measured 2-theta range was 5 – 90°, with a step size of 0.02° and a divergence slit of 1°. X-ray wavelength was 1.78897 nm. A small amount of sample was powdered manually and smeared evenly on to a glass slide with ethanol, then allowed to air dry. Pattern interpretation was completed using the Bruker DIFFRAC.SUITE EVA software package. Peak displacement, caused by slight variations in the absolute sample-detector geometry, was corrected for by aligning the measured quartz diffraction peaks at around 24° and 31° 2-theta angles. Pure samples were spiked with a small amount of powdered quartz to provide measureable quartz diffraction peaks to aid alignment.

Relative changes in lattice parameters for epidote, pumpellyite and prehnite were determined by measuring the shift in position of specific diffraction peaks (Bayliss *et al.* 1980). In epidote, the *b* axis

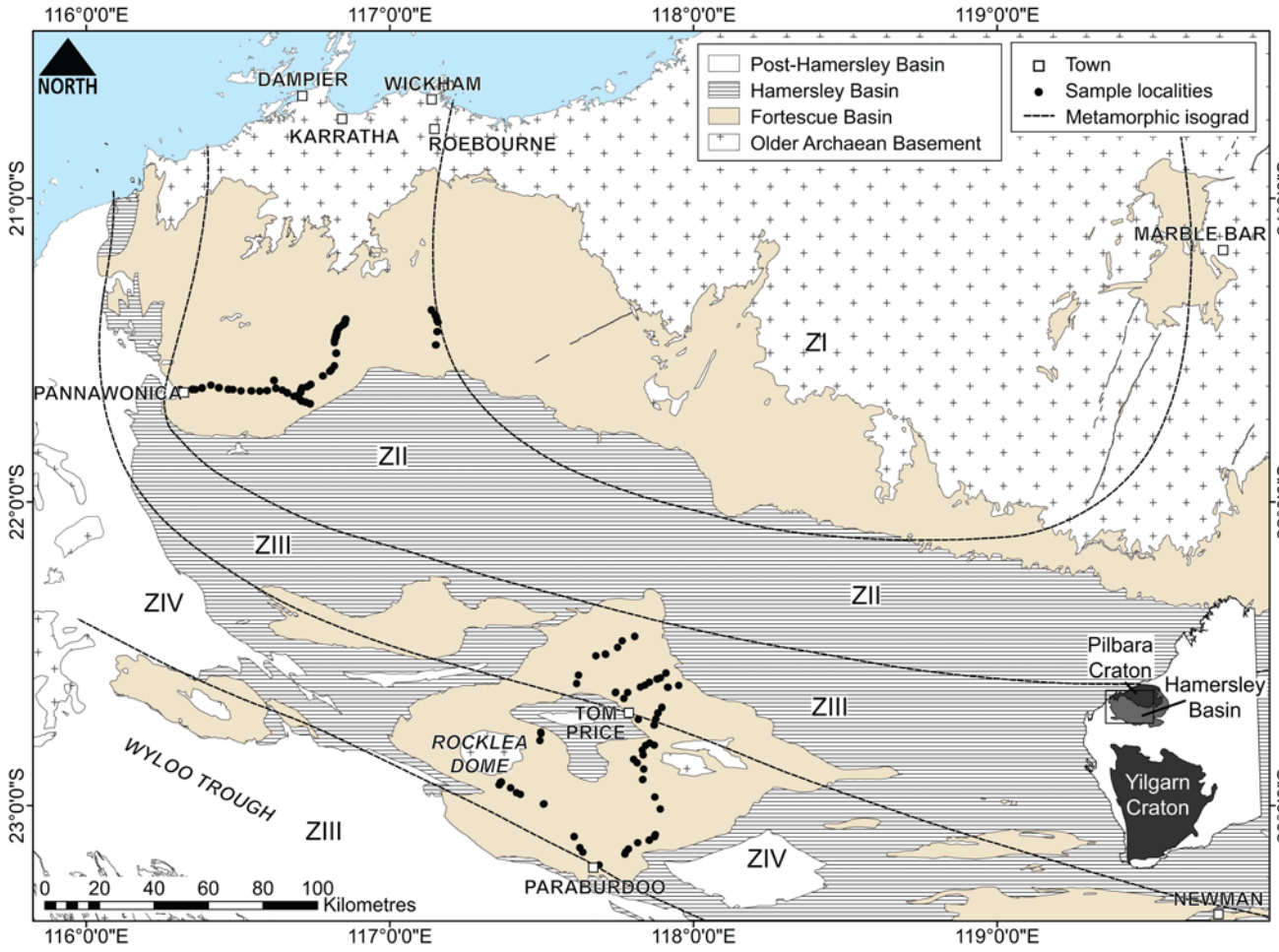

Fig. 4. A simplified geological map of the Hamersley Basin, showing the distribution of the Fortescue Group, the regional metamorphic isograds of Smith *et al.* (1982), and the locations of samples collected as part of this study (White *et al.* 2014*a*). Metamorphic ZI, prehnite–pumpellyite; ZII, prehnite–pumpellyite–epidote; ZIII, pumpellyite–epidote–actinolite–prehnite; ZIV, epidote–actinolite.

shows the greatest change with varying composition (Franz & Liebscher 2004), so the (020) peak at around 37° 2-theta was used. For pumpellyite, the high intensity diffraction peak at around 36° 2-theta was used, which corresponds to the (115) plane. For prehnite, the (111) peak at around 29.8° 2-theta was used. Plotted uncertainties for XRD peak positions are based on the resolution of the instrument (0.02°) and consequently represent a minimum estimate of the total uncertainty.

For all measured samples, spectra were compared against the Crystallography Open Database (Gražulis *et al.* 2009) to determine

Table 2. *Sources of samples used in this study*

	Sample Source	Sample Location
Epidote		
M1384	Mitchell Collection, CSIRO	Mont Cornillon, Oisans, Isere, France
M1618	Mitchell Collection, CSIRO	Val Malenco, Italy
MDC3842	Mineral Division Collection, WA Museum	Mt. Edon, Western Australia
MDC4155	Mineral Division Collection, WA Museum	Mt. Edon, Western Australia
MT8330	Mitchell Collection, CSIRO	Nahant, Essex County, Massachusetts, USA
'HM-*' samples	This study	Fortescue Group, Pilbara, Western Australia
Pumpellyite		
M332-1996	WA Museum	Paynes Find, Mid West Region, Western Australia
S1721	Simpson Collection, WA Museum	Ubini, Mid West Region, Goldfields-Esperance, Western Australia
'HM-*' samples	This study	Fortescue Group, Pilbara, Western Australia
Prehnite		
M1369	Mitchell Collection, CSIRO	Prospect, New South Wales, Australia
M1370	Mitchell Collection, CSIRO	Somerville, Massachusetts, USA
MDC1455	Mineral Division Collection, WA Museum	Dooley Downs Homestead, Gascoyne, Western Australia
MDC3799	Mineral Division Collection, WA Museum	Beebyn Station, Mid West Region, Western Australia
S1253	Simpson Collection, WA Museum	Ord River, East Kimberley, Western Australia
S1255	Simpson Collection, WA Museum	Paterson, New Jersey, USA
'HM-*' samples	This study	Fortescue Group, Pilbara, Western Australia

Table 3. *Results of EPMA, XRD and FTIR analysis of epidote, pumpellyite and prehnite samples*

Sample ID	Composition		XRD (2θ°)		FTIR (nm)		FTIR (relative depth)	
Epidote	Xep	±σ	d(020)	Abundance (%)	ν(OH)	2ν(OH)	ν(OH)	2ν(OH)
M1384	0.82	0.01	37.02	*100*	2965.54	1546.20	0.41	0.0061
M1618	0.72	0.01	37.06	*100*	2965.37	1547.63	0.35	0.0366
MDC3842	0.87	0.01	36.91	*100*	2964.84	1544.82	0.33	0.0058
MDC4155	0.90	0.01	36.98	*100*	2963.05	1545.58	0.12	0.0066
MT8330	0.81	0.01	37.03	*100*	2964.8	1545.86	0.31	0.0079
HM-3C	0.39	0.01	37.19	13.37	2972.65	1552.10	0.20	0.0019
HM-6A	0.33	0.01	37.22	18.10	2974.68	1553.34	0.24	0.0022
HM-9C	0.36	0.01	37.21	nd	nd	nd	nd	nd
HM-11	0.37	0.01	37.21	15.84	2971.77	1551.81	0.24	0.0028
HM-12A	0.35	0.01	37.25	18.95	2975.79	nd	0.30	nd
HM-12C	0.52	0.01	37.13	6.19	2973.4	1551.60	0.19	0.0015
HM-13B	0.36	0.01	37.25	nd	nd	nd	nd	nd
HM-15	0.41	0.01	37.20	12.79	2974.09	1552.73	0.24	0.0022
HM-29D	0.44	0.01	37.22	nd	2970.04	nd	0.26	nd
HM-29E	0.54	0.01	37.16	nd	2965.59	nd	0.23	nd
HM-29H	0.38	0.01	37.22	8.34	2973.76	1552.70	0.20	0.0022
HM-50B	0.39	0.01	37.21	nd	nd	nd	nd	nd
HM-50D	0.36	0.01	37.21	18.36	2967.87	1552.65	0.25	0.0012
HM-68A	0.66	0.01	37.10	nd	2966.79	1547.65	0.19	0.0014
HM-71D	0.74	0.01	37.05	nd	2967.49	nd	0.16	nd
HM-89	0.82	0.01	37.00	36.77	2965.5	1544.61	0.35	0.0030
HM-101F	0.76	0.01	36.97	nd	2963.77	1546.52	0.31	0.0009

							Band A-a		Band B-b		Band C-c		Band D-d		Band A-a		Band B-b		Band C-c		Band D-d	
Pumpellyite	X(Mg)	±σ	X(Fe)	±σ	d(115)	Abundance (%)	ν(OH)	2ν(OH)	ν(OH)	2ν(OH)	ν(OH)	2ν(OH)	ν(OH)	2ν(OH)	ν(OH)	2ν(OH)	ν(OH)	2ν(OH)	ν(OH)	2ν(OH)	ν(OH)	2ν(OH)
M332-1996	0.82	0.01	0.01	0.01	36.04	*100*	2754.11	1416.83	2815.72	1434.15	2939.81	1464.20	3139.38	1511.25	0.29	0.0023	0.24	0.0017	0.31	0.0025	0.30	0.0030
S1721	0.70	0.01	0.00	0.02	35.95	*100*	2755.16	1416.83	2816.29	1433.99	2935.27	1464.81	3136.61	1512.05	0.25	0.0047	0.15	0.0050	0.24	0.0068	0.24	0.0117
HM-12A	0.45	0.01	0.00	0.01	35.97	24.98	2730.95	nd	2817.07	nd	2937.12	nd	3153.97	nd	0.03	nd	0.28	nd	0.27	nd	0.29	nd
HM-20A	0.55	0.01	0.00	0.01	35.99	nd	nd	nd	nd	nd	nd	nd	nd	nd	nd	nd	nd	nd	nd	nd	nd	nd
HM-20C	0.65	0.01	0.01	0.01	35.97	8.69	2740.29	1412.13	2811.55	1431.13	2944.56	nd	nd	1511.14	0.26	0.0032	0.32	0.0008	0.14	nd	nd	0.0011
HM-20E	0.52	0.01	0.00	0.01	35.98	48.51	2746.72	1412.17	2815.97	1432.36	2929.83	1465.28	3152.80	1510.75	0.18	0.0017	0.46	0.0017	0.52	0.0036	0.43	0.0066
HM-21D	0.53	0.01	0.00	0.01	35.97	36.59	2752.06	nd	nd	nd	nd	nd	nd	nd	0.19	nd	nd	nd	nd	nd	nd	nd
HM-22A	0.60	0.03	0.00	0.03	35.97	8.64	2741.74	nd	2814.87	nd	2940.98	nd	3142.60	nd	0.28	nd	0.29	nd	0.17	nd	0.05	nd
HM-23C	0.33	0.01	0.00	0.01	35.95	11.14	2742.55	nd	2814.02	nd	2939.99	nd	3183.32	nd	0.28	nd	0.34	nd	0.20	nd	0.07	nd
HM-29D	0.49	0.01	0.05	0.01	35.93	27.23	2738.90	1412.46	2814.81	1433.35	2934.50	1460.49	3154.33	1512.06	0.17	0.0036	0.42	0.0010	0.36	0.0028	0.23	0.0026
HM-29E	0.46	0.01	0.08	0.01	35.92	33.77	2745.59	nd	nd	nd	nd	nd	nd	nd	0.23	nd	nd	nd	nd	nd	nd	nd
HM-50D	0.51	0.01	0.02	0.01	35.96	21.30	2731.53	1413.53	2814.70	nd	2936.30	1462.62	3145.45	1511.39	0.08	0.0017	0.33	nd	0.28	0.0010	0.22	0.0031
HM-63C	0.36	0.01	0.06	0.01	35.94	26.87	2749.98	nd	2809.97	nd	2953.45	nd	3156.02	nd	0.07	nd	0.23	nd	0.15	nd	0.24	nd
HM-71D	0.40	0.01	0.03	0.01	35.93	11.98	2745.84	1410.57	2813.02	1430.69	2930.63	nd	3142.60	1513.66	0.38	0.0024	0.32	0.0014	0.19	nd	0.12	0.0010
HM-75A	0.33	0.01	0.05	0.01	35.94	9.29	2739.95	1412.48	2814.10	1431.42	2944.31	1464.64	nd	1512.25	0.30	0.0038	0.34	0.0012	0.15	0.0011	nd	0.0008
HM-101F	0.46	0.01	0.02	0.01	35.96	30.27	2736.29	1412.36	2816.09	1430.73	2936.85	1460.34	3171.70	1511.29	0.08	0.0017	0.39	0.0011	0.38	0.0019	0.24	0.0031

Prehnite	X(Fe)	± σ	d(111)	Abundance (%)	ν(OH)	2ν(OH)		
M1369	0.16	0.01	29.75	*100*	2854.85	1476.33	0.85	0.146
M1370	0.05	0.02	29.79	*100*	2856.05	1476.39	0.89	0.107
MDC1455	0.00	0.05	29.86	*100*	2855.33	1476.80	0.67	0.007
MDC3799	0.13	0.01	29.82	*100*	2853.68	1476.57	0.81	0.056
S1253	0.14	0.01	29.77	*100*	2853.94	1476.58	0.63	0.037
S1255	0.16	0.01	29.82	*100*	2856.78	1476.78	0.88	0.084
HM-20C	0.04	0.03	29.85	10.41	nd	nd	nd	nd
HM-20G	0.02	0.04	29.86	5.38	2859.92	1477.30	0.08	0.005
HM-23C	0.04	0.03	29.84	7.09	2859.92	1477.25	0.05	0.004

Xep = $Fe^{3+}/(Al + Fe^{3+} + Cr^{3+} - 2)$, X(Mg) = $Mg/(Mg + Fe^{2+})$, X(Fe) = $Fe^{3+}/(Fe^{3+} + Al)$, 'nd', not determinable. XRD abundance data from White (2013) and 'nd' typically indicates abundances less than *c.* 5%.

semi-quantitative mineral abundances. Mineral proportion (vol. %) determinations are generally considered reliable to a precision of *c.* 5 vol. %.

Electron probe microanalysis

Mineral chemical data were obtained using a JEOL 8530F Hyperprobe Field Emission Gun Electron Probe Microanalyser (EPMA), fitted with five wavelength dispersive spectrometers, at the Centre for Microscopy, Characterisation, and Analysis at the University of Western Australia. An accelerating voltage of 15 kV, beam current of 10 nA and spot size of 2 μm were used in all cases. Data were processed using the Probe for EPMA software package. Measurements were made on samples prepared as polished thin sections. Analyses used in this study are averages of multiple measurements (typically greater than 10) made on each sample. Epidote and prehnite analyses were recalculated on the basis of 12.5 and 11 oxygens respectively, assuming all Fe was Fe_2O_3. Pumpellyite analyses were recalculated on the basis of 16 cations per 24.5 oxygens, following the formula of Coombs *et al.* (1976), with Fe^{3+} estimated via charge balance. Uncertainties on compositional parameters are determined from propagated EPMA counting statistics, given at 1 sigma.

Fourier transform infrared spectroscopy

Reflectance spectra were obtained on a Bruker Vertex 70 Fourier Transform Infrared (FTIR) Spectrometer fitted with a gold, 562-G Bruker integrating sphere. Powdered samples were placed in a black cup holder at the base of the integrating sphere. The footprint of the light source on the sample holder is *c.* 5 mm in diameter. The same aliquot of powdered sample was used for both XRD and FTIR analysis. MIR spectra were collected between 5000 – 650 cm^{-1} (2000 – 15 380 nm), at a resolution of 4 cm^{-1}, averaged over 256 scan integrations. All measurements were made using a liquid nitrogen cooled MCT detector, a KBr beam-splitter and SiC Globar light source. SWIR spectra were collected between 8000 – 4000 cm^{-1} (1250 – 2500 nm) using a resolution of 4 cm^{-1}, 128 scans, InGaAs detector, CaF_2 beam-splitter and a tungsten halogen lamp light source. A pure gold standard was used to assess for noise, instrument artefacts and atmospheric (air in the instrument) interference. Plotted uncertainties for IR feature positions are based on the resolution of the instrument (4 cm^{-1}, which corresponds to *c.* 1 nm at 1250 nm and *c.* 100 nm at 15 380 nm) and consequently represent a minimum estimate of the total uncertainty.

Both MIR and SWIR spectra were analysed using The Spectral Geologist (TSG™) HotCore software package. 'Base reflectance' spectra presented below are the raw reflectance spectra collected by the spectrometer. 'Hull removed' spectra are those that have had the background continuum removed in the TSG software. The wavelength positions of absorption features were determined individually, due to the small total number of samples, by manually comparing visual estimates with polynomial fitting algorithms in TSG using the hull removed spectra. This was deemed more reliable than using automated unmixing algorithms in TSG, which are susceptible to errors associated with the identification of minor spectral features if the search range is incorrectly defined.

Results

For each of the investigated calc-silicate minerals (i.e. epidote, pumpellyite and prehnite) in each sample, EPMA compositions are compared with XRD peak positions, and the wavelength positions and relative depths of the hydroxyl related stretching fundamentals, ν(OH), and their corresponding first overtone modes, 2ν(OH), in the

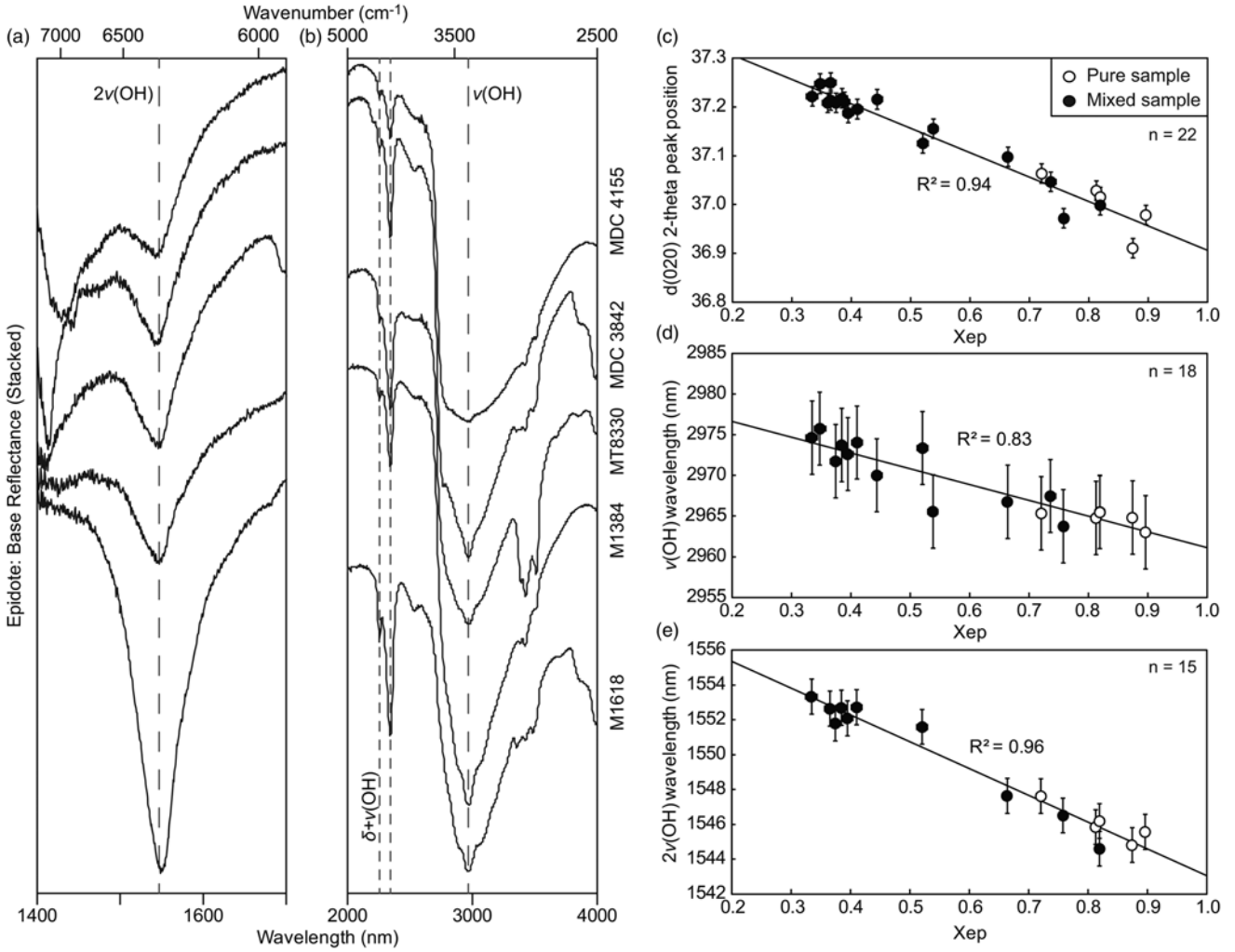

Fig. 5. Results of FTIR, EPMA and XRD analysis of epidotes. SWIR (**a**) and SWIR-MIR (**b**) reflectance spectra of pure sample epidotes show well defined characteristic ν(OH) and 2ν(OH) absorption features, as well as the positions of the δ + ν(OH) bend plus stretch combinations. EPMA compositions show strong correlations with XRD (**c**) and FTIR (**d** – MIR, **e** – SWIR) data with a shift towards shorter absorption wavelengths and larger lattice parameters with increasing Fe content. Xep = $Fe^{3+}/(Al + Fe^{3+} + Cr^{3+} - 2)$. Differing numbers of data points in **c**–**e** are due to difficulties identifying distinct absorption features in mixed mineral samples. Reflectance spectra are stacked and reflectance values are not to scale.

MIR and SWIR ranges respectively. Results are presented graphically in Figures 5, 6 and 7, and in Table 3. Averaged mineral data for the pure samples analysed in this study are given in Table 4. Mineral data for epidote and pumpellyite from mixed mineral samples in the Fortescue Group are provided by White (2013) and White *et al.* (2014*a*). Prehnite analyses from mixed mineral samples are also given in Table 4. Table 5 provides a summary and compares the results of this study with previous data. Where correlation coefficients (R^2) are given below and in figures, these exclude uncertainties. In certain mixed mineral samples from the Fortescue Group, the position of particular infrared absorption features could not be determined (denoted as 'nd' in Table 3) either due to low mineral abundance causing negligible absorption, or due to interference of other mineral phases. This latter situation is discussed further below.

Epidote

Infrared, XRD and EPMA results for analysed epidotes are presented in Figure 5. Analysed epidote samples cover a range of compositions from Xep 0.3 – 0.9 (Xep = $Fe^{3+}/[Al + Fe^{3+} + Cr^{3+} - 2]$) (Fig. 5c and e). Samples are clustered towards the two ends of this range, with few analyses falling in the range Xep 0.45 – 0.7, which is consistent with a well-documented miscibility gap in the clinozoisite – epidote solid solution (Raith 1976). The compositional range is dominated by mixed samples from the Fortescue Group, which is similar to that seen across the entire Hamersley Basin (White 2013; White *et al.* 2014*a*). In contrast, the pure samples typically have the most ferric compositions, although there is still some overlap in compositional range between pure and mixed mineral samples, such that the trends and correlations described below are considered reliable.

XRD data show a variation in the position of the d(020) diffraction peak at around 37° 2-theta (Fig. 5c), which correlates strongly with EPMA compositions ($R^2 = 0.94$); *c.* 37.25° 2-theta at Xep = 0.3 and 36.95° 2-theta at Xep = 0.9. This is consistent with expansion of the crystal lattice due to the inclusion of Fe.

In the MIR range, epidote is characterized by ν(OH) at around 2990 nm (3345 cm^{-1}; Langer & Raith 1974) (Fig. 5b; Table 5). The wavelength position of this ν(OH) shifts to shorter wavelengths (higher frequencies) with increasing EPMA-determined Fe content ($R^2 = 0.83$); *c.* 2975 nm (3360 cm^{-1}) at Xep = 0.3, and 2963 nm (3375 cm^{-1}) at Xep = 0.9 (Fig. 5d). The relative depth of this ν(OH) feature correlates strongly with XRD-determined mineral abundance in mixed mineral samples ($R^2 = 0.88$; not presented here in graphical form). Pure mineral samples display variable absorption depths although in general they are all deeper than the mixed mineral samples.

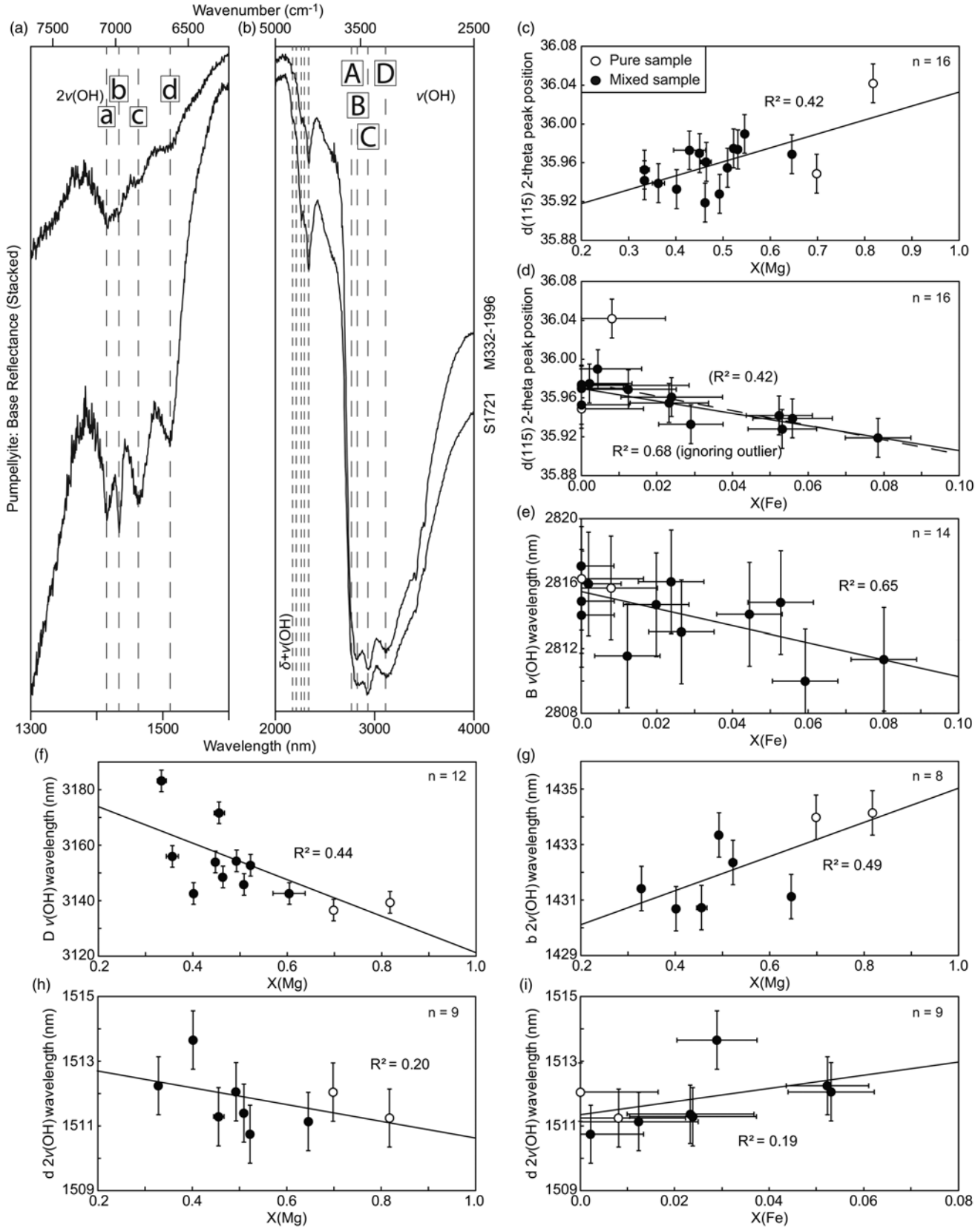

Fig. 6. Results of FTIR, EPMA and XRD analysis of pumpellyites. SWIR (**a**) and MIR (**b**) spectra of pure sample pumpellyites show well defined characteristic absorption features. XRD data show no significant correlation with X(Mg) [Mg/(Fe^{2+} + Mg)] (**c**) and only a tentative correlation with X(Fe) [Fe^{3+}/(Al + Fe^{3+})]. FTIR data (**e**–**i**) typically show weak to moderate correlations with EPMA compositions, particularly X(Mg). Differing numbers of data points in **c**–**i** are due to difficulties identifying distinct absorption features in mixed mineral samples. Reflectance spectra are stacked and reflectance values are not to scale.

In the SWIR range, epidote is characterized by 2ν(OH) at around 1550 nm (6450 cm^{-1}) (Fig. 5a; Roache *et al.* 2011). As with the fundamental feature, the wavelength position of this overtone shifts towards shorter wavelengths with increasing Fe content (R^2 = 0.96); 1553 nm (6440 cm^{-1}) at Xep = 0.3, 1545 nm (6472 cm^{-1}) at Xep = 0.9 (Fig. 5e). There is consequently a strong correlation

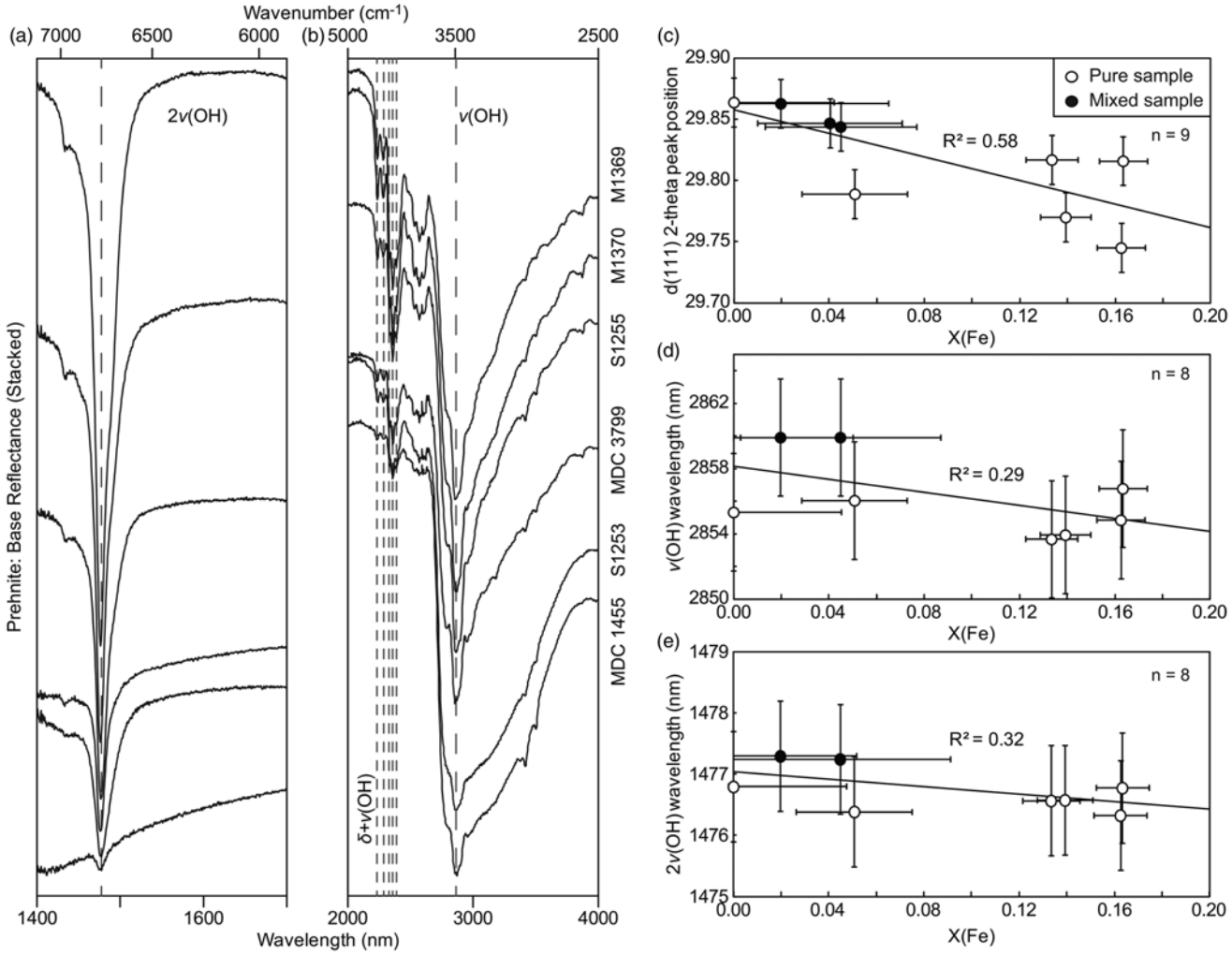

Fig. 7. Results of FTIR, EPMA and XRD analysis of prehnites. SWIR (**a**) and MIR (**b**) spectra of pure sample prehnites show well defined characteristic ν(OH) and 2ν(OH) absorption features, as well as the positions of the δ + ν(OH) bend plus stretch combinations. EPMA compositions show a moderate correlation with XRD (**c**), towards larger lattice parameters with increasing Fe content, but there is no statistically significant correlation with FTIR (**d** – MIR, **e** – SWIR) data over the range of measured compositions. The dashed line in d represents the best fit line through all data, including the outlier, whereas the solid line excludes the outlier. X(Fe) = $Fe^{3+}/(Al + Fe^{3+})$. Differing numbers of data points in **c**–**e** are due to difficulties identifying distinct absorption features in mixed mineral samples. Reflectance spectra are stacked and reflectance values are not to scale.

between the wavelengths of absorption features in the MIR and SWIR ranges ($R^2 = 0.93$; not presented here in graphical form). The relative depth of this 2ν(OH) feature shows a moderate correlation with XRD-determined mineral abundance in mixed mineral samples ($R^2 = 0.30$; not presented here in graphical form). Again, pure mineral samples have variable absorption depths that are generally deeper than for mixed mineral samples.

Theoretically, 2ν(OH) overtones should fall at double the frequency of the fundamental vibration, plus an anharmonicity factor, which describes the departure of the potential energy curve of a given bond from a parabola (Banwell & McCash 1995). The wavelength position of the measured 2ν(OH) overtone at around 1550 nm (6450 cm^{-1}) requires anharmonicities of around 280 cm^{-1}. Calculated anharmonicities show a general correlation with composition ($R^2 = 0.65$; not plotted here), with a smaller anharmonicity at higher Fe contents. Such a correlation between composition and anharmonicity has also been documented for calcic amphiboles (Laukamp *et al.* 2012).

Combination δ + ν(OH) vibrations occur at around 2250 nm (4445 cm^{-1}) and 2340 nm (4375 cm^{-1}) (Fig. 5b). These are typically well-defined features, although they coincide with δ + ν(OH) features in other associated minerals such as chlorite and calcic amphiboles (Doublier *et al.* 2012; Laukamp *et al.* 2012).

The results of this study are consistent with the findings of Langer & Raith (1974) and Roache *et al.* (2011) regarding the positions of the ν(OH) fundamental and 2ν(OH) overtone in epidote, along with their shift with composition (Table 5). The shift of infrared absorption features to shorter wavelengths with the replacement of Al by Fe is opposite to that expected from considerations of cation electronegativity (Martínez-Alonso *et al.* 2002). Langer & Raith (1974) used the observed shift in ν(OH) fundamental position to determine a lengthening of the O10–H···O4 bridge. This is interpreted to weaken the hydrogen bond and allow the hydroxyl group to vibrate at higher frequencies.

Pumpellyite

Infrared, XRD and EPMA results for analysed pumpellyites are presented in Figure 6. Two important compositional parameters are considered for pumpellyite: X(Mg) = [Mg/(Fe^{2+} + Mg)] and X(Fe) = [$Fe^{3+}/(Al + Fe^{3+})$]. Available samples cover a range of X(Mg) values from *c.* 0.3 – 0.8 (Fig. 6c). The majority of analyses are from mixed mineral samples with X(Mg) values in the range 0.3 – 0.6. X(Fe) shows a more restricted compositional range from 0 to 0.08 (Fig. 6d). There is a weak correlation between X(Mg) and X(Fe) values such that more Fe-rich samples tend to be enriched in both

Table 4. *Averaged mineral analyses for pure epidote, pumpellyite and prehnite samples and prehnite analyses from mixed mineral samples*

Sample ID Mineral	M1384 Epidote	M1618 Epidote	MDC3842 Epidote	MDC4155 Epidote	MT8330 Epidote	M332-1996 Pumpellyite	S1721 Pumpellyite	M1369 Prehnite	M1370 Prehnite	MDC1455 Prehnite	MDC3799 Prehnite	S1253 Prehnite	S1255 Prehnite	HM-20C Prehnite	HM-20G Prehnite	HM-23C Prehnite
Wt % Oxides																
SiO_2	38.70	39.29	38.55	38.50	38.63	36.33	38.39	43.58	44.40	44.44	43.90	44.09	43.72	45.61	44.72	44.70
TiO_2	0.07	0.06	0.01	0.02	0.13	0.02	0.01	0.03	0.00	0.01	0.01	0.01	0.01	0.07	0.04	0.02
Al_2O_3	23.20	24.43	22.57	22.42	23.31	25.24	24.56	19.95	23.07	24.37	20.49	20.23	19.91	24.19	24.72	23.98
Cr_2O_3	0.01	0.00	0.01	0.00	0.01	0.00	0.00	0.00	0.00	0.00	0.00	0.01	0.00	0.03	0.00	0.00
Fe_2O_3	12.80	11.36	13.86	14.37	13.05	nd	nd	6.11	1.97	0.07	5.02	5.19	5.99	1.67	0.96	1.85
FeO	nd	nd	nd	nd	nd	1.50	1.87	nd	nd	nd	nd	nd	nd	nd	nd	nd
MnO	0.00	0.00	0.07	0.00	0.00	0.15	0.01	0.00	0.00	0.01	0.00	0.00	0.00	0.02	0.03	0.02
MgO	0.00	0.02	0.01	0.00	0.05	3.05	2.45	0.01	0.00	0.00	0.00	0.00	0.00	0.12	0.03	0.00
CaO	22.69	23.02	22.29	22.50	22.78	22.52	22.56	25.92	26.32	26.04	25.52	25.48	26.07	26.36	26.14	25.92
Na_2O	0.01	0.01	0.01	0.01	0.01	0.00	0.01	0.02	0.00	0.09	0.08	0.09	0.01	0.04	0.03	0.04
K_2O	0.00	0.00	0.00	0.01	0.00	0.00	0.00	0.00	0.00	0.01	0.01	0.00	0.00	0.01	0.02	0.01
H_2O	1.90	1.91	1.89	1.89	1.89	6.67	6.66	4.29	4.36	4.40	4.32	4.32	4.29	4.38	4.38	4.37
Total	97.48	98.19	97.38	97.83	97.97	88.81	89.86	95.62	95.76	95.04	95.03	95.10	95.71	98.12	96.69	96.54
Cations																
Si	3.07	3.08	3.08	3.06	3.06	6.04	6.35	3.05	3.05	3.05	3.07	3.08	3.06	3.05	3.03	3.04
Ti	0.00	0.00	0.00	0.00	0.01	0.00	0.00	0.00	0.00	0.00	0.00	0.00	0.00	0.00	0.00	0.00
Al	2.17	2.26	2.12	2.10	2.18	4.95	4.79	1.65	1.87	1.97	1.69	1.67	1.64	1.91	1.97	1.92
Cr^{3+}	0.00	0.00	0.00	0.00	0.00	0.00	0.00	0.00	0.00	0.00	0.00	0.00	0.00	0.00	0.00	0.00
Fe^{3+}	0.77	0.67	0.83	0.86	0.78	0.04	0.00	0.32	0.10	0.00	0.26	0.27	0.32	0.08	0.05	0.09
Fe^{2+}	nd	nd	nd	nd	nd	0.17	0.26	nd	nd	nd	nd	nd	nd	nd	nd	nd
Mn	0.00	0.00	0.00	0.00	0.00	0.02	0.00	0.00	0.00	0.00	0.00	0.00	0.00	0.00	0.00	0.00
Mg	0.00	0.00	0.00	0.00	0.01	0.76	0.60	0.00	0.00	0.00	0.00	0.00	0.00	0.01	0.00	0.00
Ca	1.93	1.93	1.91	1.92	1.93	4.02	4.00	1.94	1.94	1.92	1.91	1.91	1.95	1.89	1.90	1.89
Na	0.00	0.00	0.00	0.00	0.00	0.00	0.00	0.00	0.00	0.01	0.01	0.01	0.00	0.00	0.00	0.01
K	0.00	0.00	0.00	0.00	0.00	0.00	0.00	0.00	0.00	0.00	0.00	0.00	0.00	0.00	0.00	0.00
Anions																
O pfu	12.5	12.5	12.5	12.5	12.5	24.5	24.5	11	11	11	11	11	11	11	11	11
OH pfu	1	1	1	1	1	7	7	2	2	2	2	2	2	2	2	2
Xep ($Fe^{3+}/[Al + Fe^{3+} + Cr^{3+} - 2]$)	0.82	0.72	0.87	0.90	0.81											
X(Mg) ($Mg/[Mg + Fe^{2+}]$)						0.82	0.70									
X(Fe) ($Fe^{3+}/[Fe^{3+} + Al]$)	0.26	0.23	0.28	0.29	0.26	0.01	0.00	0.16	0.05	0.00	0.13	0.14	0.16	0.04	0.02	0.04

H_2O determined from stoichiometry. $Xep = Fe^{3+}/(Al + Fe^{3+} + Cr^{3+} - 2)$, $X(Mg) = Mg/(Mg + Fe^{2+})$, $X(Fe) = Fe^{3+}/(Fe^{3+} + Al)$.'nd', not determined; 'pfu', per formula unit.

Table 5. *Summary of ν(OH) and 2ν(OH) positions in epidote, pumpellyite and prehnite determined in this study, compared with existing data*

Feature (nm)		This study	Existing Data		
Epidote			Langer & Raith (1974)	Makreski *et al.* (2007)	Roache *et al.* (2011)
ν(OH)		2963 – 2976	2970 – 3006	2972 – 3007	
2ν(OH)		1545 – 1553			1540 – 1560
δ + ν(OH)		2250, 2340			
Xep		*0.9 – 0.3*	*0.9 – 0*	*0.89 – 0*	*0.9 – 0.05*
Pumpellyite			Hatert *et al.* (2007)	Hamada *et al.* (2010)	Nagashima *et al.* (2010)
A	ν(OH) (nm)	2730 – 2755			
a	2ν(OH)	1411 – 1417			
?	ν(OH)		2858		
B	ν(OH)	2810 – 2817	2823	2847	2839
b	2ν(OH)	1431 – 1434			
C	ν(OH)	2930 – 2953	2935	2943	2959
c	2ν(OH)	1460 – 1465			
D	ν(OH)	3137 – 3183	3198	3105	3205
d	2ν(OH)	1511 – 1514			
?	ν(OH)		3322	3435	3279
δ + ν(OH)		2170, 2205, 2260, 2295, 2335			
X(Mg)		*0.8 – 0.3*	*0*	*0.88 – 1*	*0.98*
X(Fe)		*0 – 0.08*	*0*	*0 – 0.01*	*0.03*
Prehnite			Gangi Reddy *et al.* (2005)	Detrie (2008)	Clark *et al.* (2007)
ν(OH)		2854 – 2860		2865	2875
2ν(OH)		1476 – 1477	1386		1480
δ + ν(OH)		2235, 2280, 2333, 2358, 2384			
X(Fe)		*0 – 0.16*	*0.05 – 0.07*	*0.07 – 0.24*	

Compositional ranges, where known, are included for reference and are shown in italics. Pumpellyite analyses from Hatert *et al.* (2007); Hamada *et al.* (2010) and Nagashima *et al.* (2010) have been recalculated using the same method as in this study to provide consistency.

Fe^{2+} and Fe^{3+}, based on the compositional recalculation scheme used. The two pure samples lie at the high X(Mg) and low X(Fe) ends of these ranges.

XRD data show a small variation in the position of the d(115) diffraction peak at around 36° 2-theta, between 35.92° and 36.00°, with an additional outlier at 36.04°. There is no statistically significant correlation with X(Mg) (Fig. 6c). The calculated correlation coefficient ($R^2 = 0.42$) is dominated by the single outlier with a large d(115) 2-theta angle. A more robust relationship is present with X(Fe) ($R^2 = 0.42$ for all data points; $R^2 = 0.68$ ignoring the outlier) in which increasing Fe content results in a decrease in the d(115) 2-theta angle, as with epidote (Fig. 6d). This is resolvable despite the limited X(Fe) range.

In the MIR range, pumpellyite displays a complex set of overlapping absorption features in the ν(OH) region, between *c.* 2730 – 3450 nm (3000 – 3635 cm^{-1}) (Fig. 6b). At least four distinct absorption features are visible with other tentative shoulders also present. The four major features comprise a weak shoulder around 2745 nm (3640 cm^{-1}), two narrow, sharp bands at around 2815 and 2935 nm (3550 and 3410 cm^{-1}), and a broader band at around 3125 nm (3200 cm^{-1}). These are labelled A, B, C and D respectively in Figure 6b.

In the SWIR range, a similar arrangement of features is seen with four distinct 2ν(OH) bands: two narrow, sharp features at around 1415 nm (7065 cm^{-1}) and 1430 nm (6995 cm^{-1}), and two broader, shallower features at 1460 nm (6850 cm^{-1}) and 1512 nm (6615 cm^{-1}). These are labelled a, b, c and d respectively in Figure 6a. In contrast to the fundamentals, the longest wavelength feature in the SWIR typically forms a distinct absorption trough, rather than a shoulder. Calculation of 2ν(OH) wavelength positions indicates anharmonicity factors of around 42 cm^{-1} for bands A–a, 25 cm^{-1} for bands B–b, 0 cm^{-1} for bands C–c, and −60 cm^{-1} for bands D–d.

The negative anharmonicity factors for bands D-d indicate that the 2ν(OH) features occur at shorter, rather than longer, wavelengths than would be predicted from a simple doubling of the ν(OH) absorption frequency. The exact reason for this is not obvious, however, complex water absorption features (from both bound and atmospheric sources) occur in the region around 3350 – 3550 nm, which results in depression of the spectra around them. Therefore, it is possible that the band D feature is being identified at longer wavelengths due to the presence of water. While every attempt has been made to minimize this when interpreting the spectra, the effect of water cannot be ruled out.

The majority of ν(OH) and 2ν(OH) features show no resolvable correlation with either X(Mg) or X(Fe) compositional parameters. In the case of X(Fe), this may be due to the limited compositional range of the samples in this study, as for prehnite. The absorption features that do show weak correlations with EPMA compositions are shown in Figure 6e–i. ν(OH) band B shifts from around 2817 to 2811 nm with increasing X(Fe) ($R^2 = 0.65$) (Fig. 6e). ν(OH) band D shifts from around 3180 nm to 3140 with increasing X(Mg) ($R^2 = 0.44$) (Fig. 6f). 2ν(OH) band b shifts from around 1430 to 1434 nm with increasing X(Mg) ($R^2 = 0.49$) (Fig. 6g). 2ν(OH) band d shifts between *c.* 1514 and 1511 nm with increasing X(Mg) ($R^2 = 0.20$) (Fig. 6h) but in the opposite direction with increasing X(Fe) ($R^2 = 0.19$) (Fig. 6i).

Bands B, C, b, c, and d show moderate to strong correlation between relative absorption depth and XRD-determined mineral abundance in mixed mineral samples, with bands C-c showing the strongest correlation: band B, $R^2 = 0.28$; band C, $R^2 = 0.79$; band b, $R^2 = 0.39$; band c, $R^2 = 0.76$; band d, $R^2 = 0.94$ (not plotted graphically here). In contrast, bands A, D, and a show no discernible correlation. This may be related to the difficulty in correctly measuring absorption in shoulder-like (band A) and broad (band D) features. Band a is also likely influenced by the presence of water around 1400 nm.

Pumpellyite displays at least five distinct δ + ν(OH) combination features in the range 2170 – 2335 nm (4280 – 4610 cm^{-1}) with sharp features occurring at 2170 nm (4610 cm^{-1}), 2260 nm

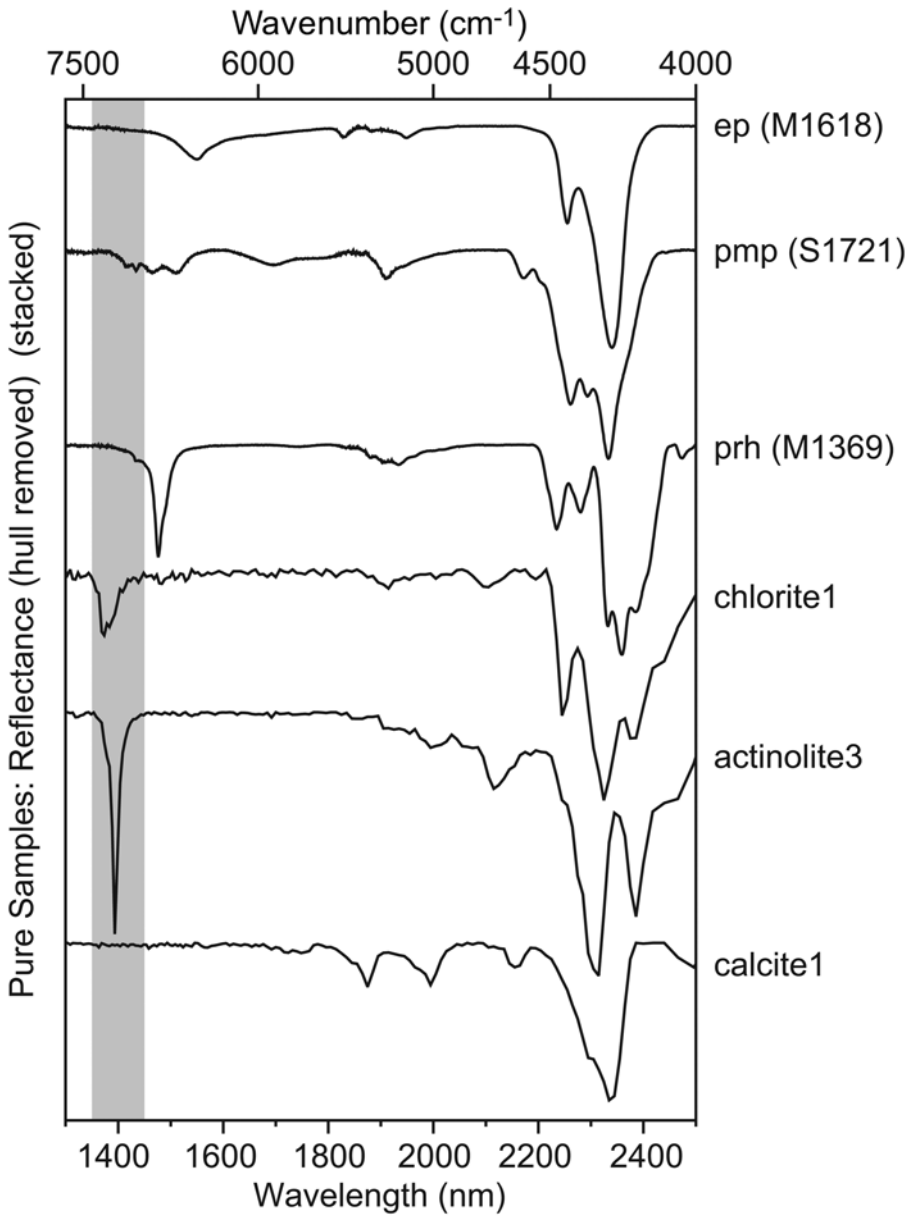

Fig. 8. Comparison of SWIR spectral signatures (continuum removed) of epidote (ep M1618), prehnite (prh M1369), pumpellyite (pmp S1721), chlorite, actinolite and calcite. The top three samples are part of the database collected for this project, whereas the bottom three spectra are from the USGS spectral library (Clark *et al.* 2007). Grey shaded band represents the main atmospheric water vapour absorption region.

(4425 cm^{-1}), 2295 nm (4357 cm^{-1}), and 2335 nm (4280 cm^{-1}), with an additional shoulder at around 2205 nm (4535 cm^{-1}) (Fig. 6b).

Overall, pumpellyite samples analysed in this study consistently show four distinct absorption features in each of the MIR and SWIR regions, corresponding to ν(OH) and 2ν(OH) respectively. Some of these features are broadly comparable to previous studies, given that many of those studies investigated pumpellyites with very different compositions to those considered here (Table 5). Only four of the absorption features (bands B, D, b, d; Fig. 6) show a resolvable shift with changing X(Mg) or X(Fe), These are typically to only a small degree, and are at the limit of spectral resolution of the FTIR detectors used in this study. In general those features that vary with composition shift towards longer wavelengths with increasing Fe content. In contrast, band b shifts towards shorter wavelengths with increasing Fe content, which may indicate the involvement of a lengthening hydrogen bond, as for epidote. Despite the observed spectral shifts described here, there is an apparent lack of significant spectral variation with changing composition, certainly when compared to epidote. However, the presence of four ν(OH) and four 2ν(OH) features is characteristic of Al–Mg–Fe pumpellyite and is useful for identification purposes. Due to the limited data set size and lack of structural refinement data no attempt is made to assign absorption bands to specific hydroxyl groups within the pumpellyite structure.

Prehnite

Infrared, XRD and EPMA results for analysed prehnites are presented in Figure 7. Analysed samples cover a limited range of compositions from approximately X(Fe) [$Fe^{3+}/(Al + Fe^{3+})$] 0.00 – 0.16 (Fig. 7c and e). Measurable mixed samples from the Fortescue Group are particularly Fe-poor.

XRD data do show a slight variation in the position of the d(111) diffraction peak between *c.* 29.74° 2-theta at X(Fe) = 0.16 and 29.86° 2-theta at X(Fe) = 0.00 ($R^2 = 0.58$), again consistent with expansion of the crystal lattice as Fe is incorporated (Fig. 7c). However, this shift in wavelength position is only just resolvable over the available compositional range.

In the MIR range, prehnite displays a ν(OH) fundamental at around 2860 nm (3496 cm^{-1}) with a broad shoulder to longer wavelengths (Fig. 7b; Detrie 2008). In the SWIR range, prehnite has a sharp, well-defined 2ν(OH) at around 1477 nm (6770 cm^{-1}) (Fig. 7a). The positions of these features vary on the order of a few

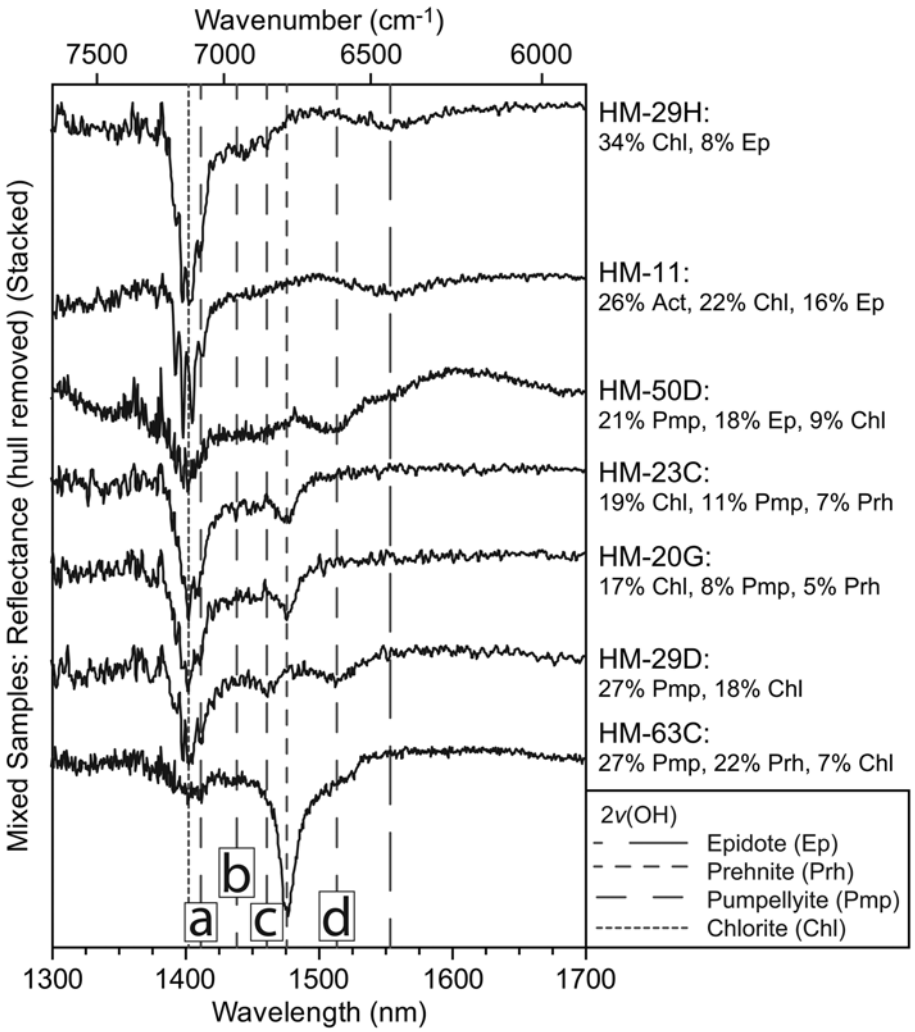

Fig. 9. Comparison of SWIR spectra of selected mixed mineral samples to illustrate the effect of mineral mixtures on the identification of 2ν(OH) features in calc-silicate minerals. Hull-removed reflectance spectra are stacked and reflectance values are not to scale. Semi-quantitative mineralogy is from XRD interpretation.

nanometres, and as such neither show a statistically significant correlation between wavelength position and EPMA compositions (MIR $R^2 = 0.29$; SWIR $R^2 = 0.32$), given the limited compositional range and instrument resolution (Fig. 7d and e). Similarly, the limited number of mixed mineral samples make assessing the relationship between abundance and absorption feature depth difficult. Calculation of 2ν(OH) frequencies suggest anharmonicities of around 230 cm^{-1}.

Prehnite displays a rather complex set of δ + ν(OH) combination features in the range 2235 – 2405 nm (4160 – 4475 cm^{-1}), typically with five distinct features at 2235 nm (4475 cm^{-1}), 2280 nm (4386 cm^{-1}), 2333 nm (4286 cm^{-1}), 2358 nm (4240 cm^{-1}), 2384 nm (4195 cm^{-1}), most of which have additional weak shoulders to one side (Fig. 7b).

All prehnite samples in this study possess a sharp ν(OH) feature at around 2860 nm, with a 2ν(OH) overtone at around 1480 nm. The ν(OH) position is consistent with the work of Detrie *et al.* (2008), however, the 2ν(OH) position determined in this study occurs at *c.* 100 nm longer wavelength than that given by Gangi Reddy *et al.* (2005), which they located at 1386 nm. There is no readily available explanation for this difference, although given the consistency of 2ν(OH) position in this study we interpret that *c.* 1480 nm is a reliable position, which is also consistent with Clark *et al.* (2007). Although no robust shift in the positions of the ν(OH) and 2ν(OH) features is present as a function of composition, at least over the limited compositional range available in this study, the presence of such features is characteristic of prehnite and useful for phase identification.

Overall, the shifts in wavelength position associated with compositional variation in pumpellyite and prehnite (at least in the case of samples analysed in this study) are significantly smaller than those seen for other minerals, including epidote (*c.* 20 nm; Langer & Raith 1974; Roache *et al.* 2011), calcic amphiboles (*c.* 25 nm; Laukamp *et al.* 2012), white mica (*c.* 55 nm; Clark *et al.* 1990*a*; Post & Noble 1993; Duke 1994), and chlorite (*c.* 25 nm; Bishop *et al.* 2008).

Discussion

The results presented above clearly identify characteristic infrared spectral features associated with each of the investigated mineral species: epidote, pumpellyite and prehnite. The application of these spectral features in mixed mineral samples measured with proximal and remote sensing technologies is now addressed.

Impact of mineral mixtures

Epidotes from pure and mixed mineral samples compare well in terms of their correlation of d(020), ν(OH) (*c.* 2990 nm) and 2ν(OH) (*c.* 1550 nm) positions with Xep (Fig. 5), suggesting only a minimal impact of other minerals on those parameters. The 2ν(OH) feature (*c.* 1550 nm) in particular is not subject to any apparent interferences and is therefore diagnostic of epidote and can be used to determine its composition (Fig. 8), as noted by Roache *et al.* (2011). This is supported by the correlation between mineral

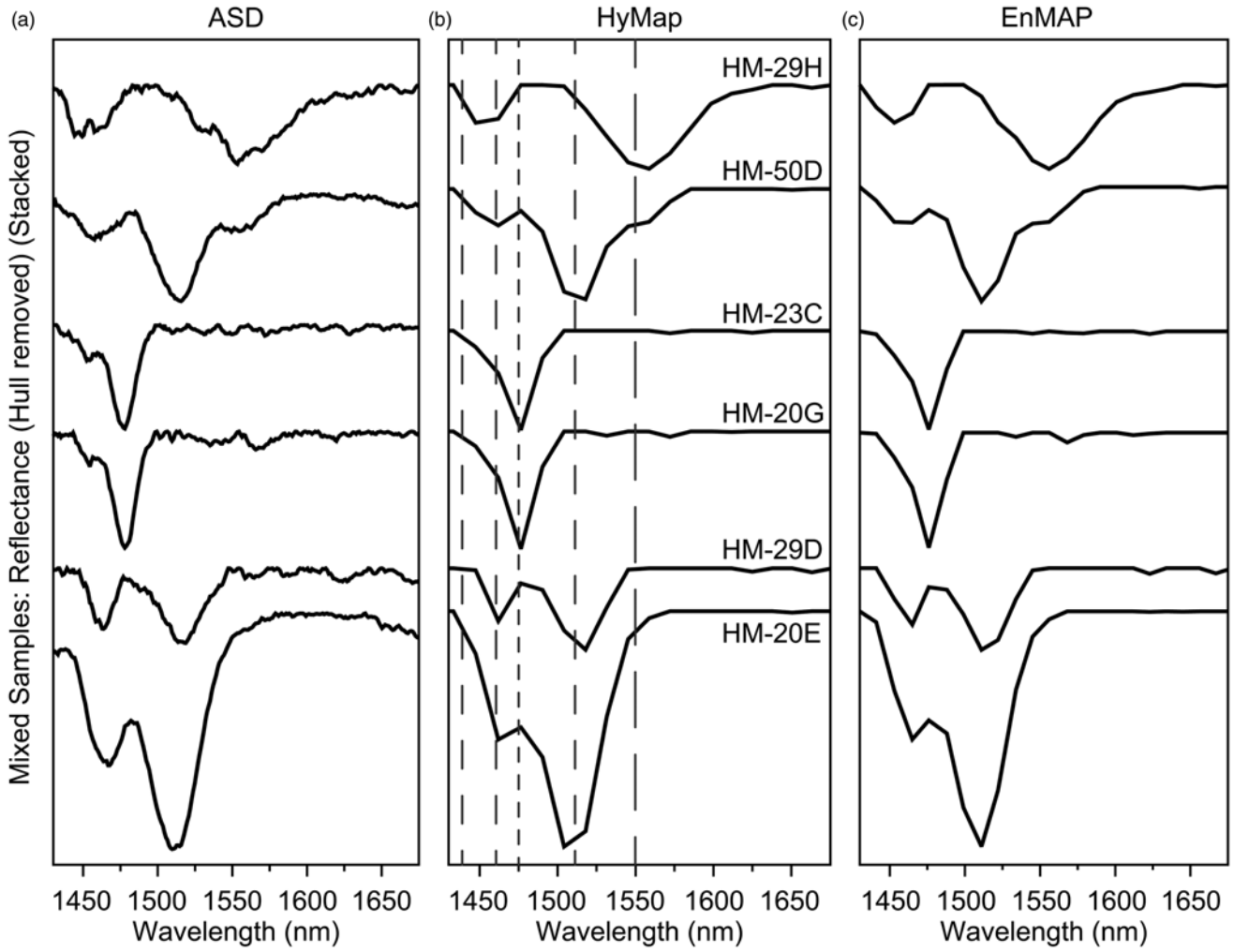

Fig. 10. Representative infrared reflectance spectra (continuum removed) of mixed mineral assemblages from the Fortescue Group, downsampled to (**a**) ASD's Field Spec Pro, (**b**) HyMap and (**c**) EnMap resolution. Dashed lines in **b** show the positions of absorption features, as per Figure 9. Semi-quantitative mineralogy from XRD interpretation: HM-29H – 34% Chl, 8% Ep; HM-50D – 21% Pmp, 18% Ep, 9% Chl; HM-23C – 19% Chl, 11% Pmp, 7% Prh; HM-20G – 17% Chl, 8% Pmp, 5% Prh; HM-29D – 27% Pmp, 18% Chl; HM-20E – 49% Pmp.

abundance and absorption feature depth in mixed mineral samples (see above; Table 3).

In general, pure and mixed samples containing pumpellyite also compare well in terms of correlations of d(115) with certain ν(OH) and certain 2ν(OH) positions with EPMA composition (Fig. 6). However, access to only two pure samples precludes a robust comparison. Pumpellyite is affected more strongly by mineral mixtures than is epidote (Fig. 9). Bands c (*c*. 1460 nm) and d (*c*. 1512 nm) are typically the strongest absorption features and can be identified in mixed mineral samples, if the proportion of pumpellyite is high (Fig. 9). As the proportion of pumpellyite drops below around 10% however, these features become increasingly more difficult to distinguish (compare samples HM-29D and HM-20G in Fig. 9). Even if the proportion of pumpellyite is high, band c can become swamped if there is a large amount of prehnite in the sample (HM-63C in Fig. 9). Band b (*c*. 1430 nm) is difficult to identify in all but pure samples. Band a (*c*. 1415 nm) is usually distinguishable, although it lies very close to the chlorite feature at around 1400 nm and may not always be reliable for use in identification. Ultimately, band d (*c*. 1512 nm) is the most reliable in determining the presence of pumpellyite in mixed mineral samples where the total proportion of pumpellyite is low. However, as shown above, the absorption depths of bands b and c show a good correlation with mineral abundance in mixed mineral samples. Therefore, these bands may be useful in estimating abundance in pumpellyite-rich samples.

Prehnites from pure and mixed mineral samples compare well in terms of ν(OH) and 2ν(OH) positions (Fig. 7). Mineral mixtures appear to have no effect on the identification of the 2ν(OH) overtone (*c*. 1480 nm), which is strong at even low prehnite contents (e.g. sample HM-20G in Fig. 9). As described above, there is an interference between band c (*c*. 1460 nm) in pumpellyite and 2ν(OH) in prehnite (*c*. 1480 nm), although in all cases prehnite dominates.

For all three minerals, δ + ν(OH) combinations overlap with those in tri-octahedral sheet-silicates (e.g. chlorite, micas) and calcic amphiboles (Doublier *et al.* 2012; Laukamp *et al.* 2012). These bands are therefore less reliable for mineral identification and determination of composition in calc-silicate minerals.

Field spectrometers and remote sensing systems

To provide a sense of which current SWIR hyperspectral technologies can be used for the characterisation of the investigated calc-silicate minerals, acquired laboratory reflectance spectra were converted to the resolution of (downsampled) (1) field spectrometer; and (2) airborne sensing resolution. Each of these systems is characterized by different wavelength coverage, spectral resolution

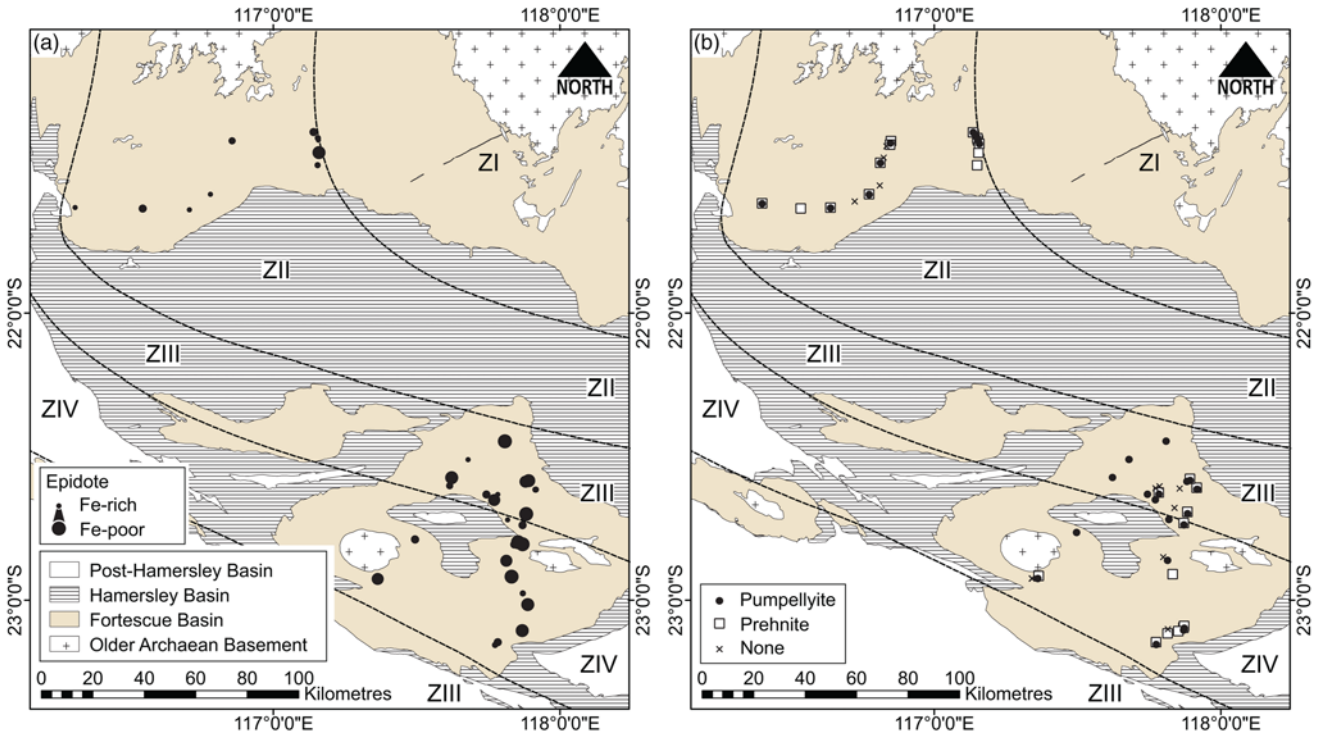

Fig. 11. The distribution of epidote (**a**), pumpellyite (**b**) and prehnite (**b**) across the Fortescue Basin, as determined by infrared spectral measurements, using the 2ν(OH) overtones of each mineral. (**a**) Circle size is proportional to the wavelength position of the epidote 2ν(OH) feature at around 1550 nm, with larger circles representing longer wavelengths and lower Fe content. There is visible trend towards decreasing Fe content with increasing metamorphic grade southwards, which agrees with EPMA compositions (White *et al.* 2014*a*). (**b**) Pumpellyite shows a decreased abundance in ZIV, other than in zones of intense metasomatism, consistent with petrographic observations (White *et al.* 2014*a*). In (**b**), overlapping symbols indicate a sample that contained both pumpellyite and prehnite. (**b**) also displays the positions of those measured samples in which none of epidote, pumpellyite or prehnite were detected.

and signal-to-noise ratio, which impacts the sensitivity of mineral characterisation. Analytical Spectral Device's (ASD) FieldSpec Pro spectrometer (Analytical Spectral Devices Inc., Boulder, CO, USA) was chosen as a representative field spectrometer, though the results can be applied to most other hyperspectral proximal sensing systems, including drill core scanning technologies (e.g. HyLogging^{TM}; Huntington 2005). For the modelling of airborne hyperspectral data, the HyMap system (Cocks *et al.* 1998) was selected. In addition, the same spectra were downsampled to the resolution of the EnMAP system (Kaufmann *et al.* 2008), which is one of the hyperspectral satellites to be launched in the near future. Current multispectral spaceborne sensors, such as ASTER (Advanced Spaceborne Thermal Emission and Reflection Radiometer; Yamaguchi *et al.* 1999) do not have a sufficient spectral resolution in the first overtone wavelength region in the SWIR and are therefore not included in this comparison.

When working with infrared remote sensing data, data for mineral mapping can only be collected in the atmospheric windows, which are those regions of the electromagnetic spectrum, particularly in the SWIR – MIR, in which atmospheric components, such as water vapour, do not obscure signals reflected from the ground. First overtones of hydroxyl-groups in most silicates are located around 1400 nm, which lies within the strong atmospheric water vapour absorption band between *c*. 1350 – 1450 nm, and therefore cannot be detected. Certain absorption bands of the investigated minerals are obscured by atmospheric features (e.g. bands a and b of pumpellyite) and, therefore cannot be identified in the field or using remote sensing technologies. Despite this, epidote, pumpellyite and prehnite can all be distinguished at the spectral resolution of the modelled proximal and remote sensing systems (Fig. 10). The 1430 – 1675 nm wavelength region shown in Figure 10 is largely unaffected by atmospheric absorption, although there is some overlap at the low wavelength end of this range below 1450 nm, and in some circumstances partial interference up to around 1500 nm. 2ν(OH) overtone bands c (*c*. 1460 nm) and d (*c*. 1512 nm) of pumpellyite (HM-29D and HM-20E in Fig. 10) are well resolved after a local continuum removal. The single major overtone absorption in prehnite, located around 1480 nm lies on the edge of the atmospheric water vapour absorption window and is well pronounced in samples HM-20G and HM-23C. However, even though both samples contain more pumpellyite than prehnite (HM-20G: 8% Pmp, 5% Prh; HM-23C: 11% Pmp, 7% Prh), only prehnite can be identified in the proximal and remote sensing data. This may be explained by the significantly more intense prehnite overtone absorption band, when compared to the shallower overtone bands of pumpellyite. The detection limit of prehnite in the SWIR is therefore much lower than that of pumpellyite.

Epidote is readily identifiable in samples HM-29H (8% Ep) and HM-11 (16% Ep) with its diagnostic overtone band located at around 1560 nm. Sample HM-50D consists of pumpellyite (21%), epidote (18%) and chlorite (9%). The pumpellyite related overtone bands c and d are pronounced, whereas the epidote related overtone is only represented by a shoulder on the longer wavelength side of band d. Wavelength shifts due to compositional variation in pumpellyite and prehnite are generally below the resolution of remote sensing techniques, although pumpellyite shifts may be detected with proximal sensing systems. In contrast, composition-driven shifts in epidote are certainly resolvable with the FieldSpec Pro spectrometer and remote sensing techniques.

In general, 2ν(OH) absorption features are generally weaker than δ + ν(OH) features for a given mineral. Here we have focussed on the 2ν(OH) as they mostly avoid issues of overlap with other minerals and can therefore be more reliable for mineral identification. However, it should be noted that in many remote sensing data sets it is possible that the 2ν(OH) absorption features may be too weak for detailed analysis beyond simple identification, particularly

in the case of pumpellyite. In contrast, proximal sensing systems should reliably be able to detect all three minerals in this wavelength range.

Mapping of epidote-pumpellyite-prehnite in the Hamersley Basin

The mineralogical and geochemical zonation observed across the Hamersley Basin is reproduced using all available FTIR measurements of 2ν(OH) overtones (only band d, *c*. 1512 nm, for pumpellyite) in sample spectra (Fig. 11). Epidote shows a broad increase in abundance (frequency of detection through spectral measurements) from ZII up to ZIV, while also showing a shift of the 2ν(OH) overtone (*c*. 1550 nm) to longer wavelengths (lower Fe content; Fig. 11a). Conversely, pumpellyite displays a decrease in abundance into ZIV where it only occurs in discrete areas, typically close to prehnite, which represent zones of metasomatism (Fig. 11b). Figure 11b also shows the positions of measured samples in which no epidote, pumpellyite or prehnite were detected. This is primarily due to those samples containing too low a proportion of epidote, pumpellyite or prehnite, instead being dominated by chlorite and/or actinolite. Although the maps in Figure 11 were produced using laboratory FTIR analyses, as discussed above, the presence of calc-silicate minerals, plus epidote composition, are likely identifiable with remote sensing systems, although prehnite and pumpellyite absorption bands may suffer from interference with atmospheric water vapour in certain circumstances.

Conclusions and applications

Our study shows that epidote, pumpellyite and prehnite have diagnostic absorption bands in the SWIR that can be used to identify their presence and possibly even their compositional variation, in terms of $Fe^{2+}Mg_{-1}$ and $Fe^{3+}Al_{-1}$ exchange. Hydroxyl-related fundamental stretching vibrations, ν(OH), of epidote, pumpellyite and prehnite are located between 2700 and 3200 nm: epidote, 2963 – 2976 nm; pumpellyite, 2730 – 2755 nm (band A), 2810 – 2817 nm (band B), 2930 – 2953 nm (band C), 3137 – 3183 nm (band D); prehnite, 2854 – 2860 nm. The respective first overtone bands, 2ν(OH), are active in the 1400 – 1560 nm wavelength region: epidote, 1545 – 1553 nm; pumpellyite, 1411 – 1417 nm (band a), 1431 – 1434 nm (band b), 1460 – 1465 nm (band c), 1511 – 1514 nm (band d); prehnite, 1476 – 1477 nm. A considerable overlap of combination bands of the hydroxyl-related stretching and bending fundamentals, δ + ν (OH) for epidote, pumpellyite and prehnite with other commonly associated minerals (e.g. tri-octahedral sheet-silicates, amphiboles, carbonates) is observed. Therefore, the first overtone bands are recommended for characterisation of these calc-silicate mineral phases. Epidote and prehnite typically produce deeper and better defined 2ν(OH) absorptions features than pumpellyite and therefore have a lower detection limit in mixed mineral samples.

Downsampling of laboratory-based FTIR measurements suggests that hyperspectral proximal and remote sensing technologies have a sufficient spectral resolution and cover the appropriate wavelength region for identification of epidote, pumpellyite and prehnite. This is demonstrated by the investigation of both pure mineral samples as well as natural samples with mixed mineral assemblages from the Fortescue Group volcanics, Hamersley Basin, Western Australia. Furthermore, mapping of calc-silicate distribution with laboratory FTIR analyses reproduces field and petrographic observations across the Hamersley Basin.

The ability to identify calc-silicate phases with hyperspectral techniques has important implications for applying remote sensing to low-grade regional metabasites. In particular, hyperspectral remote sensing tools may be useful in mapping calc-silicate mineral distribution in large igneous provinces, where such phases are common. As the distribution of calc-silicate minerals is related to metamorphic grade, such hyperspectral maps could be used directly as maps of metamorphic grade, and more importantly, to understand metamorphic gradients and metamorphic processes across large igneous provinces.

Calc-silicate minerals are also common in hydrothermally altered rocks. Therefore, hyperspectral maps of calc-silicate mineral distribution can be used to trace fluid pathways and zones of hydrothermal fluid activity. This is especially relevant where hydrothermal alteration results in the formation of mineral deposits. For example, epidote-quartz rocks commonly occur in the root zones of volcanic-hosted massive sulfide base metal deposits, locally in ophiolites (Richardson *et al.* 1987; Jowitt *et al.* 2012) and on a regional scale (Lesher *et al.* 1986; Hannington *et al.* 2003). In addition, the epidote and pumpellyite rich rocks in the Fortescue Group represent zones of significant Fe depletion, which has been speculatively associated with the upgrading of banded iron formations into economic iron ore deposits in the Hamersley Group (White *et al.* 2014*a*). Therefore, identifying zones of hydrothermal-related calc-silicates with remote sensing techniques is directly applicable to exploration for a variety of mineral deposit types, in a range of geologic settings across the world.

Finally, remote sensing applications are directly applicable to the mapping of extraterrestrial planetary surfaces. Mars orbiter instruments, as well as earlier ground-based methods, have already identified a range of mineral species on the Martian surface, including prehnite and possible pumpellyite (Clark *et al.* 1990*b*, 2008; Milliken *et al.* 2008; Mustard *et al.* 2008; Poulet *et al.* 2008; Ehlmann *et al.* 2009). Definitively identifying calc-silicate minerals on the surface has implications for understanding tectonic, metamorphic, and, more importantly, hydrosphere processes on Mars.

Acknowledgements The authors are extremely grateful to the highly constructive reviews of two anonymous reviewers. M. Verrall's assistance with sample preparation is greatly appreciated. L. Chaves and M. Iglesias are thanked for their assistance with collecting infrared spectra. The authors acknowledge the facilities, and the scientific and technical assistance of D. Adams, M. Roberts and the Australian Microscopy and Microanalysis Research Facility at the Centre for Microscopy, Characterisation and Analysis, the University of Western Australia, a facility funded by the University, State and Commonwealth governments. Detailed reviews of Edward Duke and one anonymous reviewer, as well as the useful comments of Yulia Uvarova and Ian Lau helped improve an earlier version of this manuscript.

Funding This study was funded through a CSIRO capability development fund fellowship to A. White, and facilitated via a CSIRO Minerals Down Under internship to M. Stokes.

Correction notice: The copyright first attributed to this article was incorrect.

References

Akasaka, M., Hashimoto, H., Makino, K. & Hino, R. 2003. ^{57}Fe Mössbauer and X-ray Rietveld studies of ferrian prehnite from Kouragahana, Shimane Peninsula, Japan. *Journal of Mineralogical and Petrological Sciences*, **98**, 31–40.

Alt, J., Honnorez, J., Laverne, C. & Emmermann, R. 1986. Hydrothermal alteration of a 1 km section through the upper oceanic crust, deep sea drilling project hole 504B: Mineralogy, chemistry, and evolution of seawater-basalt interactions. *Journal of Geophysical Research*, **91**, 10309–10335.

Armbruster, T., Bonazzi, P. *et al*. 2006. Recommended nomenclature of epidote group minerals. *European Journal of Mineralogy*, **18**, 551–567.

Artioli, G. & Geiger, C.A. 1994. The crystal chemistry of pumpellyite: An X-ray Rietveld refinement and ^{57}Fe Mössbauer study. *Physics and Chemistry of Minerals*, **20**, 443–453.

Artioli, G., Quartieri, S. & Deriu, A. 1995. Spectroscopic data on coexisting prehnite-pumpellyite and epidote-pumpellyite. *Canadian Mineralogist*, **33**, 67–75.

Banerjee, N., Gillis, K. & Muehlenbachs, K. 2000. Discovery of epidosites in a modern oceanic setting, the Tonga forearc. *Geology*, **28**, 151–154.

Banwell, C.N. & McCash, E.M. 1995. *Fundamentals of Molecular Spectroscopy*. McGraw-Hill, New York.

Bayliss, P., Berry, L.G., Mrose, M.E. & Smith, D.K. 1980. *Mineral Powder Diffraction File Data Book*. JCPDS International Centre for Diffraction Data, Swarthmore, PA, USA.

Bellamy, L.J. & Owen, A.J. 1969. A simple relationship between the infra-red stretching frequencies and the hydrogen bond distances in crystals. *Spectrochimica Acta*, **25A**, 329–333.

Bishop, J.L., Lane, M.D., Dyar, M.D. & Brown, J. 2008. Reflectance and emission spectroscopy study of four groups of phyllosilicates: smectites, kaolinite-serpentines, chlorites and micas. *Clay Minerals*, **43**, 35–54.

Bonazzi, P. & Menchetti, S. 1995. Monoclinic members of the epidote group: effects of $Al \leftrightarrow Fe^{3+} \leftrightarrow Fe^{2+}$ substitution and of the entry of REE^{3+}. *Mineralogy and Petrology*, **53**, 133–153.

Clark, R.N., King, T.V.V., Klejwa, M. & Swayze, G.A. 1990*a*. High spectral resolution reflectance spectroscopy of minerals. *Journal of Geophysical Research*, **95**, 12653–12680.

Clark, R.N., Swayze, G.A., Singer, R.B. & Pollack, J.B. 1990*b*. High-resolution reflectance spectra of Mars in the 2.3-μm region: evidence for the mineral scapolite. *Journal of Geophysical Research*, **95**, 14463–14480.

Clark, R.N., Swayze, G.A., Wise, R., Livo, E., Hoefen, T., Kokaly, R. & Sutley, S.J. 2007. USGS digital spectral library splib06a. *U.S. Geological Survey, Digital Data Series*, **231**, http://speclab.cr.usgs.gov/spectral.lib06.

Clark, R.N., Swayze, G.A. *et al*. 2008. Diversity of mineralogy and occurrences of phyllosilicates on Mars. *EOS, Transactions American Geophysical Union, 89(53), Fall Meeting Supplementary, Abstract P43D-04*.

Cocks, T., Jensen, R., Stewart, A., Wilson, I. & Shields, T. 1998. The HyMap airborne hyperspectral sensor: The system, calibration and performance. *In:* Schläpfer, D. & Itten, K.I. (eds) *Proceedings of the 1st EARSeL Workshop on Imaging Spectroscopy*, 6–8 October 1998, Zurich, EARSeL, Paris, 37–42.

Comodi, P. & Zanazzi, P.F. 1997. The pressure behaviour of clinozoisite and zoisite: An X-ray diffraction study. *American Mineralogist*, **82**, 61–68.

Coombs, D.S., Nakamura, Y. & Vuagnat, M. 1976. Pumpellyite-actinolite facies schists of the Taveyanne Formation near Loèche, Valais, Switzerland. *Journal of Petrology*, **17**, 440–471.

Detrie, T.A. 2008. *Prehnite at the atomic scale: Al/Si ordering, hydrogen environment, and high-pressure behaviour*. PhD Thesis, Virginia Polytechnic Institute and State University, USA.

Detrie, T.A., Ross, N.L., Angel, R.J. & Welch, M.D. 2008. Crystal chemistry and location of hydrogen atoms in prehnite. *Mineralogical Magazine*, **72**, 1163–1179.

Dollase, W.A. 1968. Refinement and comparison of the structures of zoisite and clinozoisite. *American Mineralogist*, **53**, 1882–1898.

Doublier, M.P., Roache, T. & Potel, S. 2010. Short-wavelength infrared spectroscopy: A new petrological tool in low-grade to very low-grade pelites. *Geology*, **38**, 1031–1034.

Doublier, M.P., Roache, T., Potel, S. & Laukamp, C. 2012. Short-wavelength infrared spectroscopy of chlorite can be used to determine very low metamorphic grades. *European Journal of Mineralogy*, **24**, 891–902.

Duke, E.F. 1994. Near infrared spectra of muscovite, Tschermak substitution, and metamorphic reaction process: Implications for remote sensing. *Geology*, **22**, 621–624.

Duke, E.F. & Lewis, R.S. 2010. Near infrared spectra of white mica in the Belt Supergroup and implications for metamorphism. *American Mineralogist*, **95**, 908–920.

Ehlmann, B., Mustard, J.F. *et al*. 2009. Identification of hydrated silicate minerals on Mars using MRO-CRISM: Geologic context near Nili Fossae and implications for aqueous alteration. *Journal of Geophysical Research*, **114**, E00D08, https://doi.org/10.1029/2009JE003339

Engvik, A., Mezger, K. *et al*. 2011. Metasomatism of gabbro – mineral replacement and element mobilization during the Sveconorwegian metamorphic event. *Journal of Metamorphic Geology*, **29**, 399–423.

Evarts, R. & Schiffman, P. 1983. Submarine hydrothermal metamorphism of the Del Puerto ophiolite, California. *American Journal of Science*, **283**, 289–340.

Franz, G. & Liebscher, A. 2004. Physical and chemical properties of the epidote minerals – an introduction. *Reviews in Mineralogy and Geochemistry*, **56**, 1–82.

Gabe, E.J., Portheine, J.C. & Whitlow, S.H. 1973. A reinvestigation of the epidote structure: Confirmation of the iron location. *American Mineralogist*, **58**, 218–223.

Gangi Reddy, N.C., Fayazyddin, S.Md., Rama Subba Reddy, R., Siva Reddy, G., Lakshmi Reddy, S., Sambasiva Rao, P. & Jagannatha Reddy, B. 2005. Characterisation of prehnite by EPMA, Mössbauer, optical absorption and EPR spectroscopic methods. *Spectrochimica Acta*, **62A**, 71–75.

Giuli, G., Bonazzi, P. & Menchetti, S. 1999. Al-Fe disorder in synthetic epidotes: A single crystal X-ray diffraction study. *American Mineralogist*, **84**, 933–936.

Gražulis, S., Chateigner, D. *et al*. 2009. Crystallography Open Database – an open-access collection of crystal structures. *Journal of Applied Crystallography*, **42**, 726–729.

Hamada, M., Akasaka, M., Seto, S. & Makino, K. 2010. Crystal chemistry of chromian pumpellyite from Osayama, Okayama Prefecture, Japan. *American Mineralogist*, **95**, 1294–1304.

Hannington, M.D., Santaguida, F., Kjarsgaard, I.M. & Cathles, L.M. 2003. Regional scale hydrothermal alteration in the Central Blake River Group, western Abitibi subprovince, Canada: implications for VMS prospectivity. *Mineralium Deposita*, **38**, 393–422.

Hatert, F., Pasero, M., Perchiazzi, N. & Theye, T. 2007. Pumpellyite-(Al), a new mineral from Beatrix, Belgian Ardennes. *European Journal of Mineralogy*, **19**, 247–253.

Hermann, W., Blake, M., Doyle M., Huston, D., Kamprad, J., Merry, N. & Pontual, S. 2001. Short wavelength infrared (SWIR) spectral analysis of hydrothermal alteration zones associated with base metal sulfide deposits at Rosebury and Western Tharsis, Tasmania, and Highway-Reward, Queensland. *Economic Geology*, **96**, 939–955.

Humphris, S. & Thompson, G. 1978. Hydrothermal alteration of oceanic basalts by seawater. *Geochimica et Cosmochimica Acta*, **42**, 107–125.

Hunt, G.R., Salisbury, J.W. & Lenhoff, C.J. 1973. Visible and near infrared spectra of minerals and rocks: VI. Additional silicates. *Modern Geology*, **4**, 85–106.

Huntington, J. 2005. *HyLogging analysis of two drill holes from the Goongarrie Ni laterite deposit, Kalgoorlie – Western Australia*. CSIRO, P2005/336.

Jowitt, S.M., Jenkin, G.R.T., Coogan, L.A. & Naden, J. 2012. Quantifying the release of base metals from source zones for volcanogenic massive sulfide deposits: Effects of protolith composition and alteration mineralogy. *Journal of Geochemical Exploration*, **118**, 47–59.

Kaufmann, H., Segl, K. *et al*. 2008. Environmental Mapping and Analysis Program (EnMAP) – Recent advances and status. Geoscience and Remote Sensing Symposium, 2008. IGARSS2008. *IEEE International*, **4**, 109–112.

Langer, K. & Raith, M. 1974. Infrared spectra of Al-Fe(III)-epidotes and zoisites, $Ca_2(Al_{1-p}Fe_p^{3+})Al_2O(OH)[Si_2O_7][SiO_4]$. *American Mineralogist*, **59**, 1249–1258.

Laukamp, C., Cudahy, T., Cleverley, J.S., Oliver, N.H.S. & Hewson, R. 2011*a*. Airborne hyperspectral imaging of hydrothermal alteration zones in granitoids of the Eastern Fold Belt, Mount Isa Inlier, Australia. *Geochemistry: Exploration, Environment, Analysis*, **11**, 3–24.

Laukamp, C., Cudahy, T., Thomas, M., Jones, M., Cleverley, J.S. & Oliver, N.H. S. 2011*b*. Hydrothermal mineral alteration patterns in the Mount Isa Inlier revealed by airborne hyperspectral data. *Australian Journal of Earth Science*, **58**, 917–936.

Laukamp, C., Termin, K.A., Pejcic, B., Haest, M. & Cudahy, T. 2012. Vibrational spectroscopy of calcic amphiboles – applications for exploration and mining. *European Journal of Mineralogy*, **24**, 863–878.

Lesher, C.M., Gibson, H.L. & Campbell, I.H. 1986. Composition-volume changes during hydrothermal alteration of andesite at Buttercup Hill, Noranda District, Quebec. *Geochimica et Cosmochimica Acta*, **50**, 2693–2705.

Makreski, P., Jovanovski, G., Kaitner, B., Gajović, A. & Biljan, T. 2007. Minerals from Macedonia XVIII. Vibrational spectra of some sorosilicates. *Vibrational Spectroscopy*, **44**, 162–170.

Martínez-Alonso, S., Rustard, J.R. & Goetz, A.F.H. 2002. Ab initio quantum mechanical modelling of infrared vibrational frequencies of the OH group in dioctahedral phyllosilictes. Part II: Main physical factors governing the OH vibrations. *American Mineralogist*, **87**, 1224–1234.

Milliken, R.E., Swayze, G.A. *et al*. 2008. Opaline silica in young deposits on Mars. *Geology*, **36**, 847–850.

Momma, K. & Izumi, F. 2011. VESTA 3 for three-dimensional visualization of crystal, volumetric and morphology data. *Journal of Applied Crystallography*, **44**, 1272–1276.

Mustard, J.F., Murchie, S.L. *et al*. 2008. Hydrated silicate minerals on Mars observed by the Mars Reconnaissance Orbiter CRISM instrument. *Nature*, **454**, 305–309.

Nagashima, M., Ishida, T. & Akasaka, M. 2006. Distribution of Fe among octahedral sites and its effect on the crystal structure of pumpellyite. *Physics and Chemistry of Minerals*, **33**, 178–191.

Nagashima, M., Armbruster, T. & Libowitsky, E. 2010. The hydrogen-bond system in pumpellyite. *European Journal of Mineralogy*, **22**, 333–342.

Packham, G. & Crook, K. 1960. The principle of diagenetic facies and some of its implications. *Journal of Geology*, **68**, 392–407.

Passaglia, E. & Gottardi, G. 1973. Crystal chemistry and nomenclature of pumpellyites and julgoldites. *Canadian Mineralogist*, **12**, 219–223.

Post, J.L. & Noble, P.N. 1993. The near-infrared combination band frequencies of dioctahedral smectites, micas and illites. *Clays and Clay Minerals*, **41**, 639–644.

Potel, S., Schmidt, S.Th. & de Capitani, C. 2002. Composition of pumpellyite, epidote and chlorite from New Caledonia – How important are metamorphic grade and whole-rock composition? *Schweizerische Mineralogische und Petrographische Mitteilungen*, **82**, 229–252.

Poulet, F., Mangold, N., Loizeau, D., Bibring, J.-P., Langevin, Y., Michalksi, J. & Gondet, B. 2008. Abundance of minerals in the phyllosilicate-rich units on Mars. *Astronomy & Astrophysics*, **487**, L41–L44.

Raith, M. 1976. The Al-Fe(III) epidote miscibility gap in a metamorphic profile through the Penninic Series of the Tauern Window, Austria. *Contributions to Mineralogy and Petrology*, **57**, 99–117.

Richardson, C.J., Cann, J.R., Richards, H.G. & Cowan, J.G. 1987. Metal-depleted root zones of the Troodos ore-forming hydrothermal systems, Cyprus. *Earth and Planetary Science Letters*, **84**, 243–253.

Roache, T.J., Walshe, J.L. *et al*. 2011. Epidote-clinozoisite as a hyperspectral tool in exploration for Archean gold. *Australian Journal of Earth Sciences*, **58**, 813–822.

Ruiz Cruz, M.D., Sanz de Galdeano, C., Alvarez-Valero, A., Rodriguez Ruiz, M. D. & Novák, J. 2010. Pumpellyite and coexisting minerals in metapelites and veins from the Federico Units in the Internal Zone of the RIF, Spain. *The Canadian Mineralogist*, **48**, 183–203.

Schmidt, D., Schmidt, S., Mullis, J., Ferreiro Mahlmann, R. & Frey, M. 1997. Very low grade metamorphism of the Taveyanne formation of western Switzerland. *Contributions to Mineralogy and Petrology*, **129**, 385–403.

Smith, R.E. 1968. Redistribution of major elements in the alteration of some basic lavas during burial metamorphism. *Journal of Petrology*, **9**, 191–219.

Smith, R.E., Perdrix, J.L. & Parks, T.C. 1982. Burial metamorphism in the Hamersley Basin, Western Australia. *Journal of Petrology*, **23**, 75–102.

Sonntag, I., Laukamp, C. & Hagemann, S. 2012. Low potassium hydrothermal alteration in low sulfidation epithermal systems as detected by IRS and XRD: An example from the Co-O mine, Eastern Mindanao, Philippines. *Ore Geology Reviews*, **45**, 47–60.

Springer, R.K., Day, H.W. & Beiersdorfer, R.E. 1992. Prehnite-pumpellyite to greenschist facies transition, Smartville Complex, near Auburn, California. *Journal of Metamorphic Geology*, **10**, 147–170.

Strens, R. 1974. The common chain, ribbon, and ring silicates. *In:* Farmer, V.C. (ed.) *The Infrared Spectra of Minerals*. Mineralogical Society, London, 305–330.

Swayze, G.A., Kokaly, R.F., Higgins, C.T., Clinkenbeard, J.P., Clark, R.N., Lowers, H.A. & Sutley, S.J. 2009. Mapping potentially asbestos-bearing rocks using imaging spectroscopy. *Geology*, **37**, 763–766.

Thorne, A. & Trendall, A. 2001. Geology of the Fortescue Group, Pilbara Craton, Western Australia. *Western Australian Geological Survey Bulletin*, **144**.

Trendall, A. 1990. Pilbara Craton, Introduction. *In: Geology and Mineral Resources of Western Australia*. Geological Survey of Western Australia Memoir, **3**, 128.

van Ruitenbeek, F.J.A., Cudahy, T., Hale, M. & van der Meer, F.D. 2005. Tracing fluid pathways in fossil hydrothermal systems with near-infrared spectroscopy. *Geology*, **33**, 597–600.

van Ruitenbeek, F.J.A., Debba, P., van der Meer, F.D., Cudahy, T., van der Meijde, M. & Hale, M. 2006. Mapping white micas and their absorption wavelengths using hyperspectral band ratios. *Remote Sensing of Environment*, **102**, 211–222.

White, A.J.R. 2013. Fortescue Group regional-scale metasomatism study. *CSIRO Data Collection*, https://doi.org/10.4225/08/51DE24218B201.

White, A.J.R., Robb, V.M., Robb, L.J. & Waters, D.J. 2010. Portable infrared spectroscopy as a tool for the exploration of gold deposits in tropical terrains: a case study at the Damang gold deposit, Ghana. *Society of Economic Geologists Special Publication*, **15**, 67–84.

White, A.J.R., Smith, R.E., Nadoll, P. & leGras, M. 2014*a*. Regional-scale metasomatism in the Fortescue Group volcanics, Hamersley Basin, Western Australia: Implications for hydrothermal ore systems. *Journal of Petrology*, **55**, 977–1009.

White, A.J.R., leGras, M., Smith, R.E. & Nadoll, P. 2014*b*. Deformation-driven, regional-scale metasomatism in the Hamersley Basin, Western Australia. *Journal of Metamorphic Geology*, **32**, 417–433.

Yamaguchi, Y., Fujisada, H., Kudoh, M., Kawakami, T., Tsu, H., Kahle, A.B. & Pniel, M. 1999. ASTER instrument characterization and operation scenario. *Advances in Space Research*, **23**, 1415–1424.

Yoshiasa, A. & Matsumoto, T. 1985. Crystal structure refinement and crystal chemistry of pumpellyite. *American Mineralogist*, **70**, 1011–1019.